Biohybrid restoration of the hippocampal loop re-establishes the non-seizing state in an in vitro model of limbic seizures

Davide Caron[a], Stefano Buccelli[b], Angel Canal-Alonso[c,d=], Narayan Puthanmadam Subramaniyam[e=], Javad Farsani[f], Giacomo Pruzzo[g], Bernabé Linares Barranco[f], Jari Hyttinen[e], Juan Manuel Corchado[c,d], Michela Chiappalone[b,h] and Gabriella Panuccio[a]*

[a] Enhanced Regenerative Medicine, Istituto Italiano di Tecnologia, Italy
[b] Rehab Technologies, Istituto Italiano di Tecnologia, Italy
[c] BISITE Research Group, University of Salamanca, Spain
[d] Institute of Biomedical Research of Salamanca, Salamanca, Spain
[e] Computational Biophysics and Imaging, Faculty of Medicine and Health Technology, Tampere University, Finland
[f] Instituto de Microelectrónica de Sevilla, IMSE-CNM (CSIC and Universidad de Seville), Spain
[g] Neuroscience and Brain Technologies, Istituto Italiano di Tecnologia, Italy
[h] Department of Informatics, Bioenegineering, Robotics and System Engineering (DIBRIS), University of Genova, Italy
[=] Equal contribution in alphabetical order.

*Correspondence to:
Gabriella Panuccio, MD, PhD
Enhanced Regenerative Medicine
Istituto Italiano di Tecnologia
Via Morego, 30
16163 Genova, Italy
email: gabriella.panuccio@iit.it

Abstract

Objective. The compromise of the hippocampal loop is a hallmark of mesial temporal lobe epilepsy (MTLE); particularly, the hippocampal output to the parahippocampal cortex is disrupted by damage of the CA1. While closed-loop deep brain stimulation (DBS) is the latest frontier to improve drug-refractory MTLE, current approaches do not restore the hippocampal loop, are designed by trial-and-error and heavily rely on seizure detection or prediction algorithms. The objective of this study is to evaluate the efficacy and robustness of bridging hippocampus and cortex via closed-loop stimulation to achieve the functional restoration of the hippocampal loop and control limbic seizures.

Approach. In hippocampus-cortex slices treated with 4-aminopyridine and in which the Schaffer Collaterals are severed, we used interictal discharges originating in the CA3 to trigger stimulation in the subiculum and re-establish the hippocampus output to the cortex. Combining tools from information theory with quantification of ictal activity, we addressed the efficacy of the bridge in restoring the functional connectivity of the hippocampal loop and controlling ictogenesis.

Main results. Bridging hippocampus and cortex recovered the functional connectivity of the hippocampal loop, controlled ictogenesis and proved robust to failure mimicking the functional impairment of the CA3 seen in MTLE rodent models and patients. The efficacy and robustness of the bridge stem in mirroring the adaptive properties of the CA3, which acts as biological neuromodulator.

Significance. A DBS device that does not depend on seizure detection/prediction algorithms but relies on endogenous interictal patterns presents the key to advance the conceptual design of current DBS paradigms for epilepsy treatment.

Keywords: Mesial temporal lobe epilepsy, Hippocampus, 4-aminopyridine, Interictal, Closed-loop stimulation, Biohybrid.

Introduction

Mesial temporal lobe epilepsy (MTLE) is the most common partial complex epilepsy in adults and the most frequently refractory to medications. While surgical ablation of the epileptic focus is the gold standard to ameliorate drug-refractory MTLE, closed-loop deep brain stimulation (DBS) is the latest frontier treatment [1], holding promise as less radical approach. Closed-loop DBS relies on seizure detection [2-4] to halt seizures, or, in more advanced paradigms, on seizure prediction [5, 6] to prevent them. The latter is more desirable for ameliorating the patient's quality of life while minimizing the sequelae of seizures [1]. However, both approaches entail the identification of unique electrographic biomarkers to inform the optimal stimulation timing, and real-time computations that add significant device complexity. Further, the plethora of existing algorithms fail in achieving 100% accuracy and sensitivity [7]. Not less important, there is still no unifying framework firmly establishing DBS parameters: similar to open-loop DBS, closed-loop devices still implement epochs of fixed-frequency stimulation, which is not grounded in physiologically relevant temporal patterns, and the stimulation policy is still based on a trial-and-error approach [8]. Most importantly, DBS aims at modifying the electrical phenotype of the brain, whereas the artificial restoration of brain circuits compromised by epilepsy is currently disregarded. As a result, DBS devices fail to act as artificial counterpart of the brain, while still being unable to offer a seizure-free life [9].

Interictal activity may present the key to devise physiologically meaningful DBS policies, since it reflects the brain's propensity to generate seizures [10, 11]. In this regard, in vitro studies using 4-aminopyridine (4AP)-treated hippocampus-cortex(CTX) slices as model of limbic ictogenesis have demonstrated that the interictal pattern generated by the hippocampal subfield CA3 controls seizure activity generated by the CTX (anti-ictogenic function) when the hippocampal loop is intact (**Figure 1, Intact loop**); likewise, Schaffer Collaterals disruption, preventing the CA3 output to the CTX, releases the ictogenicity of the latter [12] (**Figure 1, Disrupted loop**). This scenario mimics the damage/sclerosis of the CA1 hippocampal subfield that is frequently observed in MTLE patients [13]. In this setting, surrogating the frequency of the CA3-driven interictal pattern with periodic stimulation delivered downstream to the Schaffer Collaterals lesion controls cortical ictal discharges [12, 14]. Building upon the anti-ictogenic role of the CA3-driven interictal activity, recent work has demonstrated the efficacy of mimicking, in an open-loop stimulation approach, the temporal dynamics (rather than the average frequency) of this pattern [15], paving the way to an interictal-based grammar for DBS.

Another important issue in DBS is establishing the most appropriate target to deliver the stimulation. Regarding MTLE, the hippocampus is one primary candidate in preclinical [12, 16-24] and clinical research [25-35]. However, hippocampal sclerosis, which primarily strikes the CA1 [13], negatively affects the efficacy of DBS delivered to the hippocampus proper. At variance, sclerosis typically spares the subiculum [36-38], which is downstream to the CA1. Further, afferent stimulation is emerging as a more effective strategy than direct stimulation of the epileptic focus. For these reasons, numerous studies are converging toward the subiculum as stimulation target in MTLE [5, 6, 14, 15, 23], herein including recent clinical trials [32, 39].

The subiculum operates as the inhibitory gate of hippocampal output activity to the CTX [40]; however, it becomes hyperexcitable in MTLE [41, 42], reinforcing rather than dampening ictogenesis [43]. Thus, targeting this structure in DBS permits to bypass the poorly responsive sclerotic CA1, rectify subicular hyperexcitability, and recruit cortical networks via afferent stimulation.

In this scenario, a closed-loop bridging neuroprosthesis relaying the CA3 interictal pattern to the subiculum represents an intriguing and straightforward strategy to restore the functional connectivity of the epileptic hippocampus: it would bypass the need of seizure prediction algorithms and would optimize the stimulation policy, since it would rely on an existing anti-ictogenic pattern rather than on trial-and-error. Yet, the feasibility of bridging CA3 and CTX via interictal-driven stimulation of the subiculum has never been addressed.

Here, we propose a biohybrid approach to restore the hippocampus-CTX loop and control limbic ictal activity. Using 4-aminopyridine (4AP)-treated hippocampus-CTX slices in which the Schaffer Collaterals are severed, we bridge the CA3 to the subiculum via activity-dependent stimulation to entrain cortical networks, while bypassing the lesioned CA1 (artificial reconnection); as the CTX input to the hippocampus is preserved (biological pathway), this strategy establishes a biohybrid loop (**Figure 1, Reconnected loop**).

We show that the biohybrid approach effectively restores the CA3-CTX dialog and controls ictal activity; further, it exhibits robustness to failure mimicking the functional impairment of the CA3 that may accompany hippocampal sclerosis [43]. Thus, our work demonstrates the possibility for a bridging neuroprosthesis to control limbic seizures that does not depend on seizure detection/prediction algorithms, but on endogenous interictal patterns. In this, the proposed paradigm outclasses the conceptual design of current DBS approaches for epilepsy treatment and paves the way to an interictal-driven DBS.

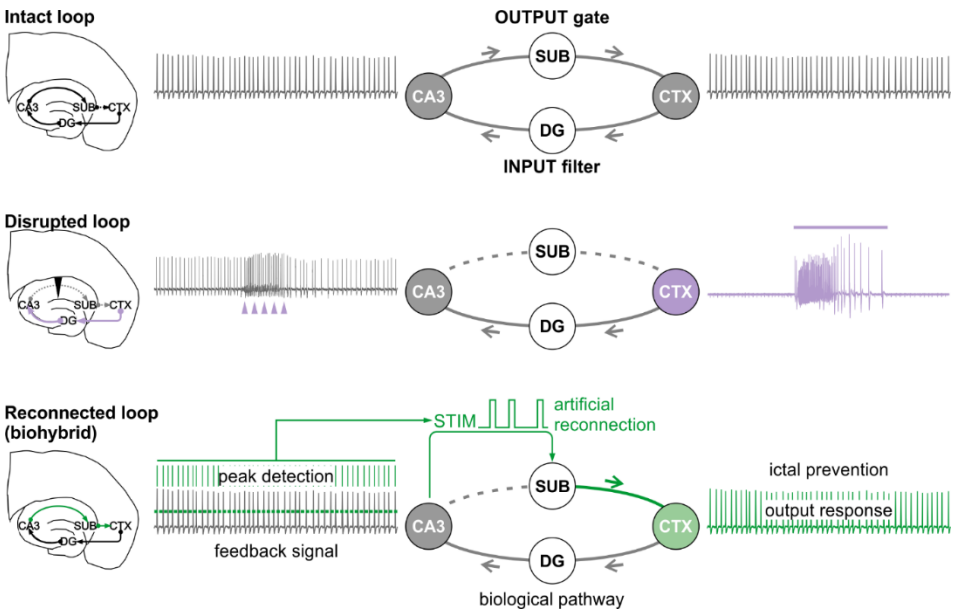

Figure 1 – Concept design of the biohybrid approach.

Schematic rendition of the CA3 and CTX interactions in the three different scenarios of intact and disrupted hippocampal loop, and upon its biohybrid restoration. On the left is the brain slice schematic representative of the different scenarios. On the right is the corresponding circuit diagram along with the electrical patterns generated by the CA3 and the CTX. In the intact hippocampal loop, the CA3 generates a fast interictal pattern that propagates to the CTX, controlling its ictogenicity. When the hippocampal loop is disrupted by Schaffer Collaterals damage (downward arrow, dashed grey line), the CA3-driven interictal pattern cannot reach the CTX; the latter generates seizure activity (solid line), which invades the hippocampus proper (arrowheads). The core concept design of the biohybrid bridging stems in forwarding the CA3-driven interictal pattern to the subiculum to recruit and entrain the CTX, bypassing the damaged Schaffer Collaterals. As this strategy surrogates the missing CA3-driven signal, it is expected to exert an anti-ictogenic function. CA3: Cornu Ammonis 3; DG: dentate gyrus; SUB: subiculum; CTX: parahippocampal CTX.

Methods

Brain slice preparation and maintenance.

Horizonal hippocampus-cortex (CTX) slices, 400 μm thick, were prepared from male CD1 mice 4-8 weeks old. Animals were decapitated under deep isoflurane anesthesia, their brain was removed within 60 s, and immediately placed into ice-cold (~2 °C) sucrose-based artificial cerebrospinal fluid (sucrose-ACSF) composed of (mM): Sucrose 208, KCl 2, KH2PO4 1.25, MgCl2 5, MgSO4, CaCl2 0.5, D-glucose 10, NaHCO3 26, L-Ascorbic Acid 1, Pyruvic Acid 3. The brain was let chill for ~2 min before slicing in ice-cold sucrose-ACSF using a vibratome (Leica VT1000S, Leica, Germany). Brain slices were immediately transferred to a submerged holding chamber containing room-temperature holding ACSF composed of (mM): NaCl 115, KCl 2, KH_2PO_4, 1.25, $MgSO_4$ 1.3, $CaCl_2$ 2, D-glucose 25, $NaHCO_3$ 26, L-Ascorbic Acid 1. After at least 60 minutes recovery, individual slices were transferred to a submerged incubating chamber containing warm (~32 °C) holding ACSF for 20-30 minutes (pre-warming) and subsequently incubated in warm ACSF containing the K+ channel blocker 4-aminopyridine (4AP, 250 μM), in which $MgSO_4$ concentration was lowered to 1 mM (4AP-ACSF, *cf.* [44]). Brain slice treatment with 4AP is known to enhance both excitatory and inhibitory neurotransmission and induce the acute generation of epileptiform discharges [45]. All brain slices were incubated in 4AP-ACSF for at least 60 minutes before beginning any recording session. All solutions were constantly equilibrated at pH = ~7.35 with 95% O_2 / 5% CO_2 gas mixture (carbogen) and had an osmolality of 300-305 mOsm/Kg. Chemicals were acquired from Sigma-Aldrich.

All procedures have been approved by the Institutional Animal Welfare Body and by the Italian Ministry of Health (authorizations 860/2015-PR and 176AA.NTN9), in accordance with the National Legislation (D.Lgs. 26/2014) and the European Directive 2010/63/EU. All efforts were made to minimize the number of animals used and their suffering.

Microelectrode array recording.

Brain slices used for closed-loop stimulation experiments were partially disconnected (*cf.* [43]); namely, the CA3 output to

the CTX was prevented by Schaffer Collateral's disruption (either during the slicing procedure or via knife cut), whereas the subicular projections to the CTX as well as the CTX input to the hippocampus were preserved. Extracellular field potentials

were acquired through a 6 x 10 planar MEA (Ti-iR electrodes, diameter 30 μm, inter-electrode distance 500 μm, impedance < 100 kΩ), in which a custom-made low-volume (~500 μl) recording chamber replaced the default MEA ring (*cf.* [44]) to attain a laminar flow. Individual slices were quickly transferred onto the recording chamber, where they were held down by a custom-made stainless steel/nylon mesh anchor. Slices were continuously perfused at ~1 ml/min with 4AP-ACSF, equilibrated with carbogen. Recordings were performed at 32° C, achieved with the use of a heating canula (PH01) inserted at the recording chamber inlet port (temperature set at 37° C) along with mild warming of the MEA amplifier base (temperature set at 32° C), both connected to a TC02 thermostat. The recording bath temperature was checked using a k-type thermocouple.

Signals were acquired with either of: **(i)** the MEA1060 amplifier using the Mc_Rack software, sampled at 2-10 kHz and low-passed at half the sampling frequency before digitization; **(ii)** the MEA2100-mini-HS60 amplifier using the Multichannel Experimenter software; the amplifier was connected to the IFB v3.0 multiboot interface board through the SCU signal collector unit; signals were sampled at 5 kHz and low-pass filtered at 2 kHz before digitization. In all experiments, signals were stored in the computer hard drive for offline analysis. The custom recording chamber was designed and made by Crisel Instruments, Italy. The equipment for MEA recording and temperature control was purchased from Multichannel Systems (MCS), Reutlingen, Germany.

Closed-loop stimulation.

In all experiments, stimulation was triggered upon detection of the CA3-driven interictal events; this was based on hard-threshold crossing of the signal amplitude, set manually for each experiment at as closely as possible to the signal baseline and no higher than one half of the maximal signal amplitude. Stimuli were delivered in the subiculum and consisted of square biphasic direct current pulses (±100-350 μA, balanced charge, 100 μs/phase, positive phase first) conveyed via MEA electrode pairs connected in bipolar configuration. As the closed-loop system operated in real-time, the delay between interictal event detection and pulse delivery was equal to the sampling interval. Supplementary Figure 1 shows a representative recording of the bridge in action, including the location of the stimulating electrode pair, the threshold used for the event detection, and the stimulus onset time (STIM).

A fast input/output (I/O) curve was always performed prior to the first stimulation protocol to find the current amplitude that would reliably elicit an interictal-like discharge (≥80% response rate, *cf.* [6, 12, 44]). The best performing stimulus amplitude was then kept constant throughout the experiment. Each stimulation session lasted at least 3 times the mean interval of occurrence of ictal discharges (as observed from the preceding control phase) and no less than 20 minutes. Baseline activity in the absence of stimulation was always recorded before and after each stimulation protocol and is overall referred to as control (CTRL).

Closed-loop architectures.

For the experiments using the MEA1060 amplifier, the closed-loop architecture was designed in Simulink environment (Mathworks, Natick, USA) receiving the MEA signals through a PCI-6255 DAQ board (National Instruments, USA), and interfaced with the MEA1060 system by a custom PCB (PCB Project, Segromigno Monte, Lucca, Italy); in this case, pulses were pre-programmed in the MC_Stimulus II software and downloaded to the STG2004 stimulus generator (both from MCS), which was triggered via TTL. Supplementary Figure 2 illustrates the Simulink model. The Analog input block reads the MEA signals through the PCI-6255 DAQ board and feeds the CA3 signal from one selected electrode to the Event detection block. The model also implements an Enabling condition for triggering the Stimulation block, to avoid multiple detections of the same event in case the CA3-driven interictal events consisted of brief population busts, and to blank the stimulus artifact that would otherwise lead to a false event detection. Specifically, we set a minimum time window of 250 ms from the last delivered pulse as the enabling condition, based on prior observation of the minimum interval of occurrence and duration of CA3-driven events and the maximum time-lag and duration of the stimulus artifact. Once triggered, the Stimulation block output, in turn, triggers the Digital Output block, which sends a TTL signal to the custom PCB controlling the external stimulator (STG2004, MCS). The Scope visualizes the MEA signals and the output of the Event detection, Time since last event, and Stimulation blocks. For the experiments using the MEA2100-mini, the closed-loop architecture relied on the built-in digital signal processor (DSP) and stimulus generator of the MEA2100 system. The DSP operates with an internal clock of 800 MHZ (1.25 ns period), while the DAC of the stimulus generator operated at 5 kHz (200 μs period).

In a subset of experiments we challenged the biohybrid paradigm against failure in pulse delivery consequent to missed detections of interictal events (hardware failure) or to mimic the CA3 functional impairment described in epileptic tissue [43].

To this end, we set up two different scenarios. In the first scenario, we set a failure rate of 50% (the closed-loop architecture would trigger a pulse every second detected event). To attain this behavior, we have first modified the Simulink model to include a hardware failure module (experiments acquired with the MEA1060 system). As illustrated in **Supplementary Figure 3**, this module is interposed between the Stimulation and the Digital Output block and implements an event counter, which is initialized at 0 and counts up to 1 to attain a 50% failure rate in triggering the Digital Output block. The module also monitors the number of delivered pulses and the number of detected events. Subsequently, this behavior was programmed directly in the built-in DSP of the MEA2100 system. In the second scenario, we set a blanking window of 5 s, during which the event detection would not trigger the stimulation. This was implemented in the MEA2100 system as a 0-current tail in the preprogrammed pulse waveform.

Data analysis.

Quantification of ictal and interictal events. Offline analysis was performed using custom software written in MATLAB R2016b or R2022a .

Ictal events were defined based on tonic-like or tonic-clonic-like signal features, disregarding duration cut-off criteria commonly used by other works in the field. Ictal activity was labeled either manually or by means of an automated seizure detection algorithm based on Daubechies discrete wavelet transform type 4 [46], followed by multiple resolution analysis (as in [15]). Detected events were confirmed/corrected by visual inspection as applicable.

To take into account the possibility of occurrence of a sole ictal discharge during electrical stimulation, ictal activity was not quantified by its duration and interval of occurrence; rather, we used the ictal state time-percentage (P_{ictal}) as indicator of the overall time spent in the ictal state during each recording phase (*cf.* [6, 47]). P_{ictal} was computed as in **Equation 1**:

Equation 1

$$P_{ictal} = \frac{\sum_{i=1}^{n} D(i)}{t_{TOT}} \times 100$$

where i is ith ictal discharge, D is the ictal discharge duration and t_{TOT} is the total observation time. For CTRL phases (no stimulation), t_{TOT} is the time between the onset of the first and the termination of the last measured ictal event; for stimulation phases (STIM), t_{TOT} is the duration of the stimulation protocol. Further, for electrical stimulation, we adopted a conservative approach by including spontaneous or evoked discharges exhibiting borderline electrographic features that could be classified neither as ictal nor as interictal events; this was done to minimize false negative bias that could yield an overestimation of the stimulation efficacy. These events are overall referred to as anomalous discharges.

Interictal activity generated by the CA3 was analyzed in terms of statistical parameters μ, σ and coefficient of variation (CV = σ/μ) of inter-event interval (IEI) distributions as follows: **(i)** events timing was retrieved using a threshold-crossing peak-detection; **(ii)**, the interictal IEIs were then fit with a lognormal using the maximum likelihood estimation method, to yield the μ, σ and CV parameters. Lognormal fit was chosen based on the previous demonstration of the lognormal temporal profile of CA3 electrical patterns [15, 48, 49]. To display the distributions, binning used the Freedman-Diaconis algorithm to account for heavy tails. This method was also applied to the analysis of inter-pulse intervals. Dissection of interictal events/pulses belonging to the interictal or ictal periods relied on previously assigned labels of ictal events.

Causality analysis. To address the causal relationship between CA3 and CTX in the two directions of the loop, we deployed two methods from information theory. The first method, Granger causality (GC), is an established approach to quantify how well one time series can be predicted from another[46]; it explores the system as a linear regression of a stochastic process to measure the amount of information transferred between two signals and yields unique characteristics of signal B inside signal A. The second method is based on ordinal partition transition networks (OPTNs); this is a relatively new approach to infer the coupling and its direction between two dynamical systems [50], which was recently extended to detect causality in multivariate observational data, such as MEA recordings, by removing non-causal nodes at various interaction delays [51].

To compute the GC, first , we used the Dickey-Fuller test to verify the non-stationarity of MEA signals, which may affect Granger causality; as the signals were indeed non-stationary, they were windowed using a 1-s hamming window to ensure accuracy and avoid artifacts. Then, Vector Auto Regressions (VAR) were fitted to each data window. To establish the model's best order, we iterated across each window using the Akaike Information Criterion. To ensure the GC calculation will not fail the VAR's model residual covariance matrix is checked to be positive definite.

Then, we calculated the GC along the VAR models of each electrode and each window, merging the final GC value in a complete time vector of each electrode, as per **Equation 2**.

Equation 2

$$X_{CTX}(t) = \sum_{j=1}^{p} A_{CTX-CTX,j} X_{CTX}(t-j) + \sum_{j=1}^{p} A_{CTX-CA3,j} X_{CA3}(t-j) + E_{CTX}(t)$$

$$X_{CA3}(t) = \sum_{j=1}^{p} A_{CA3-CTX,j} X_{CTX}(t-j) + \sum_{j=1}^{p} A_{CA3-CA3,j} X_{CA3}(t-j) + E_{CA3}(t)$$

In **Equation 2**, *p* is the model order, *A* is the matrix containing the contribution of each lagged observation to the predicted values and *E* is the prediction error in each time series (residuals). It can be said that a signal from CA3 "granger causes" a signal from CTX if the variance of E_{CTX} is reduced by the inclusion of X_{CA3}; likewise, it can be said that a signal from CTX "granger causes" a signal from CA3 if the variance of E_{CA3} is reduced by the inclusion of X_{CTX}.

Analysis was made using custom software written in MATLAB R2022a. Signals were not filtered to avoid artifacts. To compare GC values across different protocols, these were normalized to a range of 0 to 1.

To compute the OPTN-based causal interactions, MEA signals from CA3 and CTX were low-pass filtered at 40 Hz and down sampled to 2 kHz. OPTN-based causal interactions were estimated in a moving window of 100 s (200000 samples) with 1 s overlap. Taken's embedding theorem [52] was used to reconstruct the phase space and obtain the ordinal patterns. For phase space reconstruction, the embedding delay was chosen based on auto mutual-information [53], whereas the embedding dimension was set to 3 based on the data length (200000 samples/window) [51, 53, 54]. For each time window, the causality was tested for delays ranging from 1 to 100 ms in 1-ms steps. The OPTN-based causality values were then averaged over the time delays for each window and assigned to the mid-point of the window. Thus, for a pair of signals we obtained time-varying OPTN-based causality measure in the form of a N x N x W matrix, where N = 2 and W = n windows; in this matrix, the off-diagonal entries represent the causal interaction among the signals, whereas the diagonal entries represent self-connections and are ignored. Comparison of the causal strength across protocols relied on the empirical cumulative distribution function (CDF) of the OPTN-derived causality normalized to a range of 0 to 1 [51].

Statistical analysis. Throughout the text, *n* indicates the number of the specified samples. Statistical analysis was performed using custom software written in MATLAB or SPSS 20 (IBM, Armonk, NY, USA). Data was first checked for normality (Shapiro-Wilk test) and homoskedasticity (Levene's test). To compare the efficacy of different stimulation protocols as well as to compare the GC values across multiple groups, we used one-way ANOVA followed by the Games-Howell post-hoc test. For statistical comparison between two groups we used the Welch test. For pairwise comparison of the OPTN-based cumulative distributions, we used the permutation testing approach [55]. Namely, we pooled the OPTN-based causality measures from two different conditions into a single set, from which we randomly drew to two sets of values, simulating a scenario where values are drawn from the same distribution. We iterated this procedure 2000 times and computed the 1-Wasserstein distance (W1) between the CDFs for each permutation, resulting in a null distribution of W1 values. If M of the null W1 values were greater than the W1 computed from the two original CDFs, the significance was assessed based on p-value given as M/n. permutations.

Statistical significance set to $p < 0.05$. Throughout the text and figures, the p values are indicated as follows: * $p <= 0.05$; ** $p <= 0.01$; *** $p <= 0.001$.

Figures. All figures were prepared in CorelDraw X8. Electrophysiology signals and graphs originally plotted in MATLAB or Microsoft Excel were imported and edited as vector graphics. Violin plots [56] were obtained using the openly shared MATLAB function violinplot.m (Bechtold, Bastian, 2016. Violin Plots for Matlab, DOI: 10.5281/zenodo.4559847); MATLAB *.fig files were exported in pdf using the export_fig.m by Oliver J. Woodford, Yair M. Altman (https://it.mathworks.com/matlabcentral/fileexchange/23629-export_fig) before importing them in CorelDraw to preserve the 'patch' vector graphics.

Results

The bridge is feasible and effective.

Delayed stimulation is a drawback of current closed-loop DBS, because this is based on detection of abnormal brain activity within a sliding window, using complex signal processing methods [57, 58]. To enable real-time feedback operation of the bridge, early detection of interictal events is here achieved with a simple amplitude threshold-crossing approach, and triggers the stimulation within one sampling interval (see online methods). This requires a high signal-to-noise ratio and that interictal events outstand the amplitude of ictal discharges that might occur within the hippocampus proper (**Supplementary Figure 4**). While this is not always attainable in the real-world setting, the presence or absence of contaminant ictal activity will depend on the efficacy of the bridge in dampening it. **Figure 2A** shows a representative bridging experiment which prevented full-blown ictal activity; the only anomalous events were short population bursts (solid lines). Full-blown ictal discharges emerged again upon stimulus withdrawal, indicating that the efficacy of the bridge is activity-dependent. A representative case of anomalous events, pointed by the arrowhead in panel A, is shown in **Figure 2B**. These events were evoked by the stimulation and exhibited borderline electrographic features that could be classified neither as ictal nor as interictal activity; likely, they reflected temporary hyperexcitability, which, however, could not converge toward a full-blown ictal discharge because of the ongoing stimulation. As summarized in **Figure 2C**, the bridge proved highly effective, achieving an overall ictal state reduction of 91.31 ± 4.33% (ictal state % – CTRL1: 20.08 ± 1.78, bridge: 1.72 ± 0.81, CTRL2: 20.07 ± 2.19; one-way ANOVA, F(df): 43.98(2), $p < 0.001$ – bridge vs CTRL1 and CTRL2; n = 9 brain slices). Thus, not only is the bridge effective in abating ictal activity; its effectiveness supports its feasibility in the case of sub-optimal signal features of the feedback electrode.

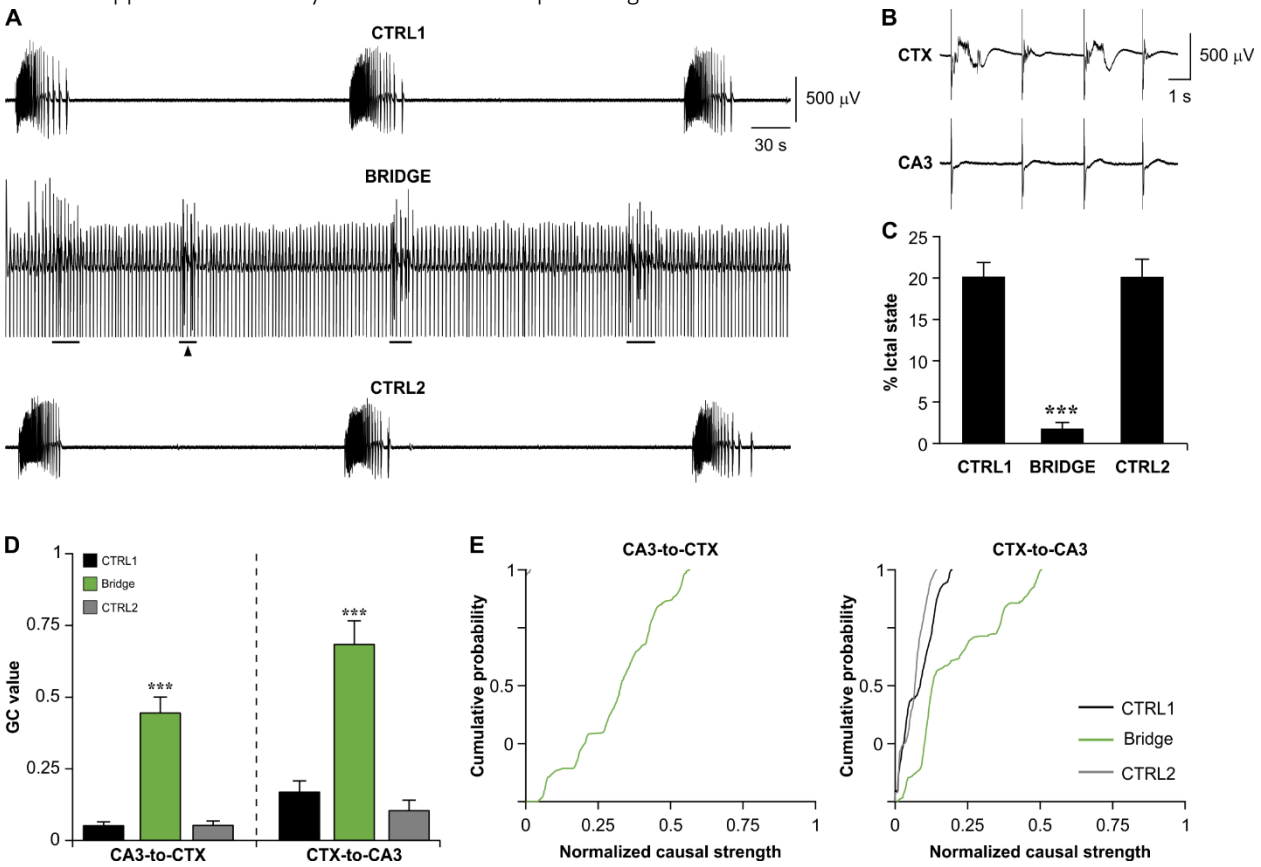

Figure 2 – Biohybrid bridging between hippocampus and CTX controls limbic ictogenesis

A. Recordings from the CTX during a representative bridging experiment. The pre-stimulus baseline (CTRL1) shows the recurrent generation of ictal discharges in the CTX; these were abolished by the bridge, during the only anomalous events were the short population bursts indicated by the solid lines. Upon stimulus withdrawal (CTRL2), the ictal events recovered to pre-stimulus condition, indicating that the effect of the bridge is activity-dependent. B. Representative case of anomalous discharges (pointed by the arrowhead in A) visualized at expanded time scale; these population bursts of borderline electrographic features represented hyperexcitable responses evoked by the stimulation. The CA3 signal serves as a reference for the pulse timings. C. Summary of the results statistics for this dataset (n = 9 brain slices), showing the high efficacy of the bridge in controlling ictal

*activity. D, E. Granger causality (D) and OPTN (E) demonstrate that the bridge induces a strong increase of the functional connectivity between CA3 and CTX in the two directions of the loop. *** p < 0.001.*

In keeping with the underlying concept of the bridge, we next sought to determine if and to what extent the bridge can restore the functional connectivity of the disrupted hippocampal loop. To this end, we deployed two methods from information theory to address the causal strength between CA3 and CTX in the two directions of the loop.

Namely, we used Granger causality (GC) [59] and ordinal partition transition networks (OPTN) [50, 51] as two methods of causality inference based on different mathematical principles: while GC measures are valid only for linear interactions, OPTN-based causality measures are sensitive to both linear and nonlinear ones; hence, their combination provides complementary information about statistically inferred coupling. As shown **Figure 2D**, the GC values demonstrated that the bridge increased the causal relationship between CA3 and CTX in the two directions of the loop (CA3-to-CTX – CTRL1: 0.05 ± 0.01; bridge: 0.44 ± 0.06; CTRL2: 0.05 ± 0.02; one-way ANOVA, F(df): 44.47(2), $p < 0.001$ bridge vs both CTRLs. CTX-to-CA3 – CTRL1: 0.17 ± 0.04; bridge: 0.68 ± 0.08; CTRL2: 0.1 ± 0.04; one-way ANOVA, F(df): 31.6(2), $p < 0.001$ bridge vs both CTRLs). This was confirmed by the right-shift of the OPTN cumulative probability curves (**Figure 2E**; see **Supplementary Table 1** for detailed statistics).

The bridge mirrors the adaptive properties of the CA3.

The functional restoration of the CA3-to-CTX connectivity is the core concept of the bridge, but it only provides a high-level rationale for its effectiveness. While the anti-ictogenic role of the CA3-driven interictal activity has been known for decades [12, 60-62], its underlying mechanism is yet unelucidated. Different studies have proposed a frequency-dependent process [12, 61], which is further supported by the demonstrated intrinsic pacemaker function of the CA3[63, 64]. Here, we hypothesized that the CA3 acts as adaptive biological neuromodulator by adapting to the cortical drive. To address this hypothesis, we first performed GC analysis in hippocampus-CTX slices before and after Schaffer Collaterals cut (n = 6 brain slices). **Figure 3A** shows a representative MEA recording from the CA3 and CTX of the same brain slice before and after disconnection. The inserts on the right show the boxed signal segments at expanded time scale to emphasize the onset and propagation (or lack thereof) of the interictal and ictal events in the two scenarios. In connected slices, the GC values confirmed the strong causality between the CA3 and CTX, which was similar in the two directions, consistent with the communication loop between these structures (CA3-to-CTX: 0.56 ± 0.01; CTX-to-CA3: 0.56 ± 0.03; $p > 0.05$, Welch test). Upon CA3-CTX disconnection, the GC values significantly dropped in both directions (CA3-to-CTX: 0.04 ± 0.01; CTX-to-CA3: 0.06 ± 0.03; $p > 0.05$, Welch test; **Figure 3B**); the drastic reduction of CA3-to-CTX causality is expected, as the pathway serving it is severed; however, the significant reduction of the CTX-to-CA3 causality is surprising, since that biological pathway is preserved. Possibly, the GC value primarily reflected the interictal periods, since they represented the largest portion of the signal. Thus, we performed a more in-depth analysis of the CTX-to-CA3 causality in disconnected brain slices, dissecting interictal and ictal epochs. As shown in **Figure 3C**, this analysis unveiled the stronger cortical drive during ictal versus interictal periods, with the latter being statistically similar to what measured for the overall signal (GC value – ictal: 0.22 ± 0.02, interictal: 0.07 ± 0.01, overall: 0.06 ± 0.03; ANOVA, F(df): 16.22(2), $p < 0.001$ ictal vs both interictal and overall signal). Consistent with this, OPTN analysis (**Figure 3D**) showed a significant drop in the directed causality in both directions upon disconnection (W_1 – CA3-to-CTX: 0.53; $p < 0.001$. CTX-to-CA3: 0.21; $p < 0.001$); further, analysis interictal and ictal epochs of disconnected brain slices unveiled the stronger cortical drive during ictal activity (W_1 – overall: 0.03; interictal: 0.004; ictal: 0.04; $p < 0.001$ ictal vs interictal/overall; **Figure 3D**, insert).

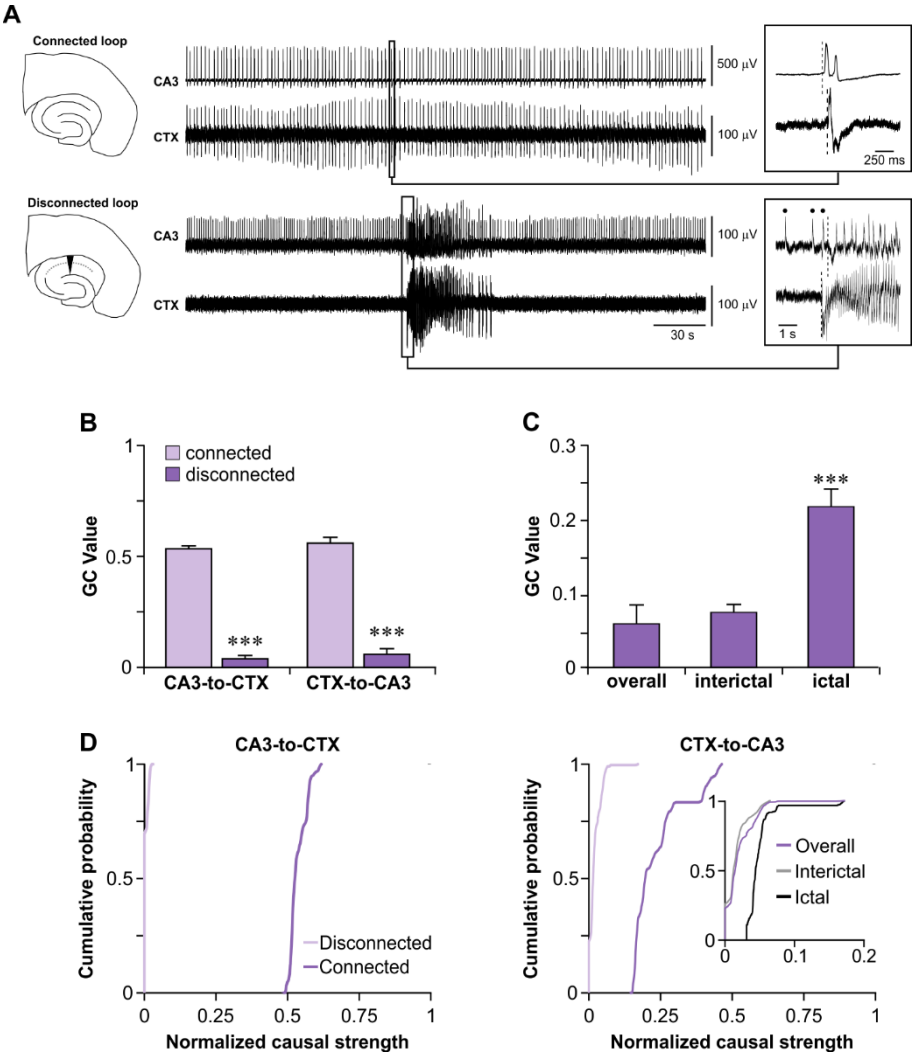

Figure 3 – Cortical ictal discharges drive the CA3 in the disrupted hippocampal loop.

*A. Representative epileptiform patterns in the CA3 and CTX of a 4AP-treated hippocampus-CTX slice before and after disconnection. Connected brain slices generate interictal events only. The insert shows the boxed interictal event at expanded time scale, to emphasize its origin in the CA3 (vertical dashed lines). Upon disconnection, the brain slice generates a mixed epileptiform pattern made of interictal and ictal activity. The boxed signal segment frames the ictal onset along with a short pre-ictal period, and is shown in the insert at expanded time scale. Note the disappearance of the CA3-driven events (dots) from the CTX and the origin of ictal activity in the latter, with subsequent propagation to the CA3 (vertical dashed lines). B. Granger causality analysis of the CA3-to-CTX and CTX-to-CA3 communication taken as the average GC value across the recorded signal. The significant drop in the GC value upon disconnection is consistent with the disruption of the CA3-to-CTX pathway, but not with the preserved CTX-to-CA3 connectivity. C. Granger causality analysis of the CTX-to-CA3 communication dissecting interictal and ictal epochs evidences the cortical drive during the latter. For clarity, the graph also shows the GC value of the overall signal reported in panel B. D. OPTN analysis confirms the absence of directed CA3-to-CTX causality, and a weak one in the CTX-to-CA3 direction in disconnected vs connected brain slices. Insert: In disconnected brain slices, the CTX-to-CA3 directed connectivity dissecting interictal and ictal epochs unveiled a stronger cortical drive during the latter. *** $p < 0.001$*

Next, we analyzed the temporal distributions of the CA3-driven interictal events in an extended dataset of disconnected brain slices (n = 59), again dissecting ictal from interictal epochs. **Figure 4A** shows a representative recording from CA3 and CTX and the distribution parameters (μ, σ, and CV = σ/μ) of inter-event intervals (IEI) demonstrating the acceleration of the CA3-driven interictal events during the ictal periods. As summarized in **Figure 4B**, this behavior was overall confirmed by population statistics (μ interictal: 1.84 ± 0.14, μ ictal: 1.38 ± 0.1, $p < 0.01$; σ interictal: 1.30 ± 0.02, σ ictal: 1.4 ± 0.03, $p > 0.01$; CV interictal: 0.89 ± 0.05, CV ictal: 1.33 ± 0.1, $p < 0.001$; Welch test).

These results anticipate that the CA3 may act as adaptive biological neuromodulator: while the disruption of the Schaffer Collaterals impede the CA3 from relaying its drive to the CTX, a CA3-driven DBS will adapt to the evolving network dynamics.

To corroborate this point, the ideal experimental scenario would be a bridge that gradually dampens rather than prevents ictal activity. This would enable to analyze the temporal distribution of the delivered pulses (hence of the CA3-driven interictal events) during the progressive abatement of ictal discharges. **Figure 5A** shows such a case: anomalous discharges are highlighted in light grey, and the pulse times (green bars) above the CTX signal emphasize the acceleration patterns during the highlighted events. In this experiment, the distribution parameters of the inter-pulse intervals initially exhibited the oscillatory trend of interictal-to-ictal transitions (*cf.* **Figure 4**); eventually, they stabilized to values similar to the ictal-free periods. The transition from the last anomalous event to the stable pattern of interictal-like evoked discharges is shown at expanded time scale in **Figure 5B**. Statistical analysis of the temporal profile of the delivered stimuli confirmed the accelerating behavior of the bridge during epochs of anomalous events (**Figure 5C**). In our hands, we encountered only one such case, because the bridge invariably exerted a strong anti-ictogenic effect. Nonetheless, this scenario suggests that the efficacy of the bridge stems in its inherent feature of relaying the CA3 adaptation to cortical inputs back to the CTX. The biological and artificial counterparts engage in a reciprocal dynamic adaptation, thereby establishing an adaptive biohybrid loop that eventually settles to a new steady-state, free of seizure activity.

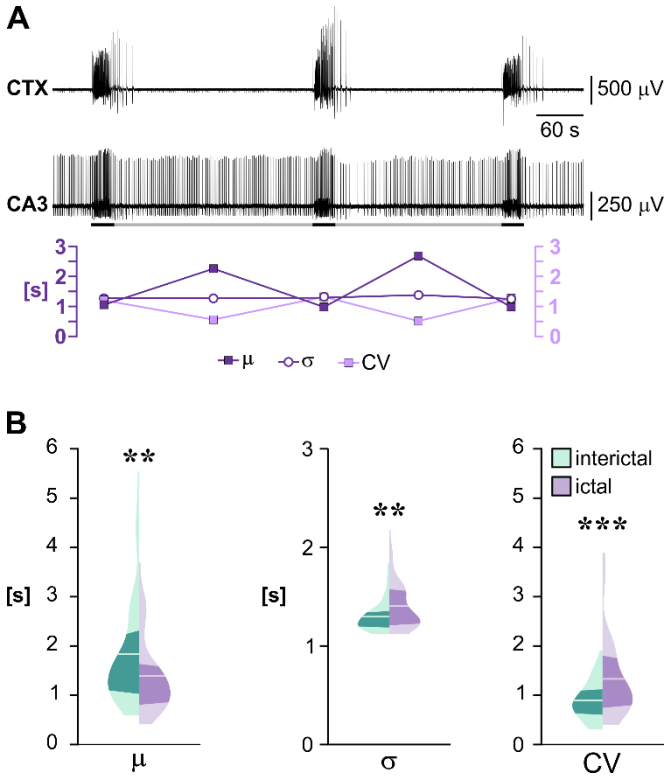

Figure 4 – The CA3 is an adaptive biological neuromodulator.

*A. Representative recording from CTX and CA3 of a disconnected brain slice showing the acceleration of the CA3-driven interictal events upon entrainment by ictal activity. The black and grey lines below the CA3 signal mark the ictal and interictal epochs, respectively, and serve as reference for the statistical parameters of the CA3 interictal temporal profile plotted below the signal. The decreased μ and CV substantiate the interictal acceleration. B. Violin plots summarizing the results statistics for the interictal temporal profile of the analyzed dataset (n = 59 brain slices), demonstrating the consistent acceleration of interictal events during epochs of ictal entrainment. The solid lines indicate the mean; the darker areas frame the quartiles. ** $p < 0.01$; *** $p < 0.001$.*

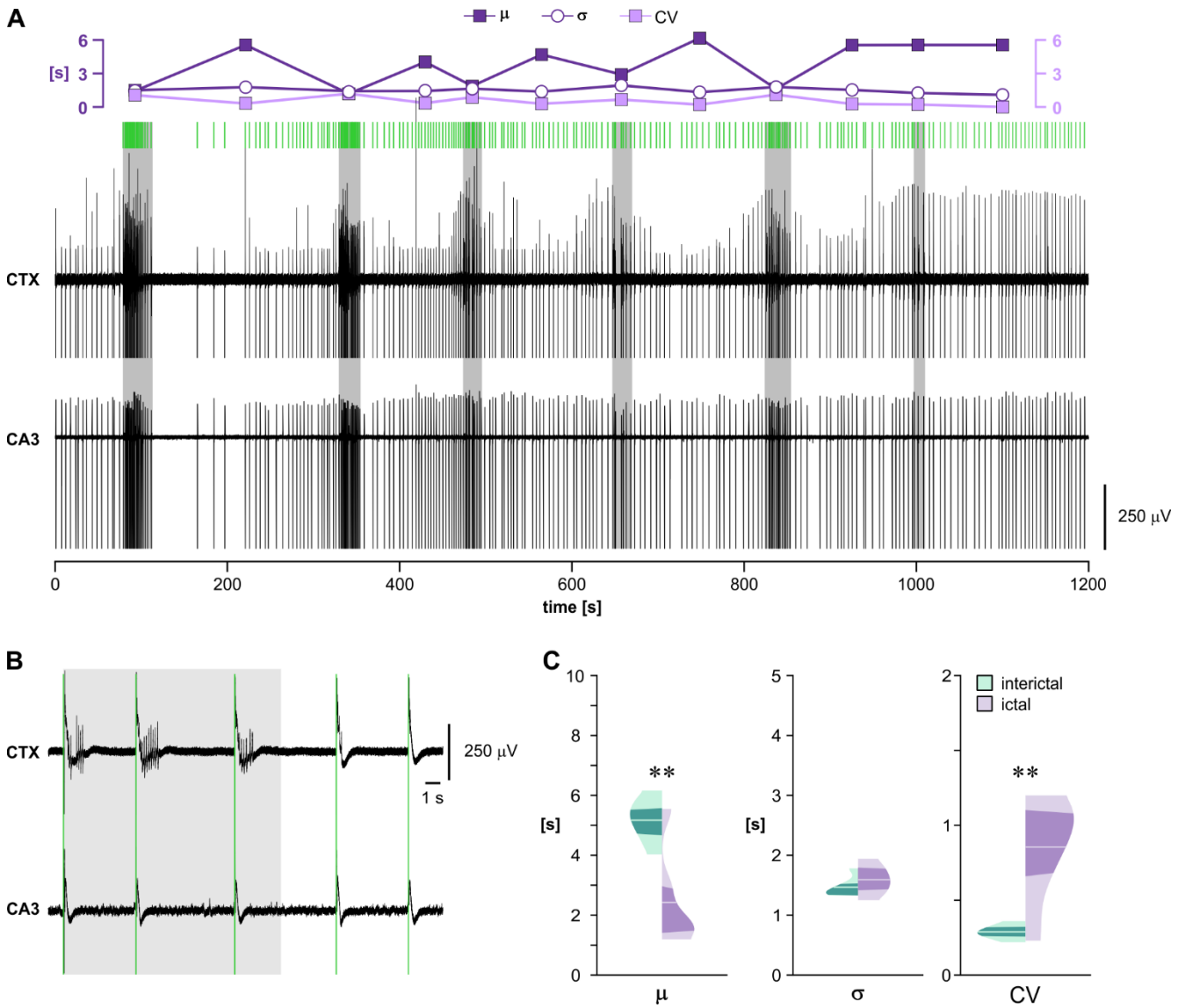

Figure 5 – The bridge mirrors the adaptive properties of the CA3.

*A. Full recording of a representative 20-minute experiment in which the bridge gradually abolished ictal activity. Stimulus artifacts are not blanked to demonstrate the operation of the bridge. Anomalous events (highlighted by the grey shading) gradually transitioned from full-blown ictal discharges to interictal-like evoked responses. The green bars above the signal mark the timings of the delivered pulses to emphasize the emerging accelerations in the CA3-driven stimuli. The insert above the signal shows the computed statistical parameters of the temporal distribution of the pulses, starting from the first labeled event: while the s parameter remained stable over time, the m parameter markedly decreased during these events; likewise, the CV parameter was higher. At the time of the last and shortest labeled event, the temporal distribution of the pulses settled to values similar to ictal-free periods. B. Recording segment starting from the onset of the last anomalous discharge in A, visualized at a faster time scale; entrainment of CTX networks by the ongoing stimulation and transition of evoked responses from population bursts to interictal-like discharges. Pulse timings are indicated by the green bars. C. Summary of the result statistics for this experiment, confirming the adaptive behavior of the bridge. ** $p < 0.01$.*

The bridge is robust to CA3 functional impairment.

The CA3 is often compromised in MTLE patients with hippocampal sclerosis [13]; in animal models, this relates with a decreased frequency of the CA3-driven interictal discharges, which is approximately halved compared to the non-epileptic control [43], posing the question of the efficacy of the bridge in such cases. Further, DBS hardware malfunction is a common cause of reappearance or worsening of symptoms in the clinical setting (15-30% of the cases [65]). To address the bridge robustness to such conditions, we challenged it against a failure rate of 50% (i.e., the stimulator delivered a pulse every second

detected event, **Figure 6A**); this paradigm is hereafter referred to as bridge-50%. In these setting, the fully efficient bridge, hereafter referred to as bridge-100%, served as positive control, and the stimulation protocols were shuffled. **Figure 6B** shows the recordings from the CTX in a representative experiment; for simplicity, we only show the bridge-50% and its related CTRL phases. In this experiment, the bridge-50% prevented the generation of full-blown ictal discharges; the only anomalous activity was a short epoch of population bursts (solid line), eventually entrained by the stimulation (**Figure 6C**). As summarized in **Figure 6D**, the bridge-50% performed similarly to the bridge-100% (n = 7 brain slices; ictal state % – pooled CTRLs: 17.67 ± 1.39; bridge-50%: 1.06 ± 0.83; bridge-100%: 0.8 ± 0.69; ictal state reduction vs preceding CTRL – bridge-50%: 92.38 ± 6.51%; bridge-100%: 95.2 ± 4.57; one-way ANOVA, F(df): 43.8(2); $p < 0.001$ for both bridges against the pooled CTRLs; $p > 0.05$ between the two bridges). Further, the effective stimulation frequency (n. pulses/stimulation duration) exhibited a variable range (0.13-0.52 Hz), which did not correlate with the degree of ictal reduction (**Figure 6E**); the mean frequency was 0.3 ± 0.06 Hz with frequencies < 0.2 Hz in ~43% of the cases. Remarkably, 0.2 Hz is the limit open-loop stimulation frequency in terms of seizure suppression efficacy regardless of the stimulation target, as demonstrated in vitro and in vivo[14, 22, 47, 66].

Granger causality (**Figure 6F**) showed that the bridge-50% improved the functional connectivity of the hippocampal loop in both directions; however, consistent with a 50% failure, the achieved functional restoration was approximately half of what achieved by the bridge-100% (GC value CA3-to-CTX – CTRL: 0.03 ± 0.01, bridge-50%: 0.23 ± 0.03, bridge-100%: 0.48 ± 0.05; ANOVA F(df): 56.5(2), $p < 0.001$ vs CTRL; $p < 0.01$ vs bridge-100%. GC value CTX-to-CA3 – CTRL: 0.1 ± 0.04, bridge-50%: 0.29 ± 0.09, bridge-100%: 0.72 ± 0.09; ANOVA F(df): 30.7(2); $p < 0.05$ vs CTRL and bridge-100%.). OPTN (**Figure 6G**) confirmed the partial restoration of the causal strength between CA3 and CTX (see **Supplementary Table 2** for detailed statistics). Yet, the achievement of ictal reduction similar to the bridge-100% and the frequency-independent efficacy indicates robustness to failure.

To further address this phenomenon, we analyzed the statistical properties of the inter-pulse intervals during the bridge-50%. **Figure 6H** shows the probability distributions for the representative case shown in panel **B**; as expected, the inter-pulse interval distribution is right-shifted compared to the distribution of the interictal IEI; remarkably, the distribution shape is fairly preserved, while the μ parameter is double the value of the interictal distribution. Comparison of the μ, σ, and CV parameters of pulse versus interictal intervals across the dataset confirmed the significant change in the μ and CV and the similarity of the σ parameter (**Figure 6I**; μ – interictal: 2 ± 0.33, pulses 4.1 ± 0.69, $p < 0.05$; σ – interictal: 1.41 ± 0.12, pulses 1.27 ± 0.07, $p > 0.05$; CV – interictal: 0.79 ± 0.11, pulses: 0.35 ± 0.05, $p < 0.01$, Welch test). Thus, the change in CV is determined by the change in the mean inter-pulse interval.

Previous analysis of a large interictal population has shown that the μ vs CV relationship of their intervals follows a power-law [15]; if the inter-pulse intervals in the bridge-50% represent a sub-population of the interictal intervals, their μ vs CV relationship should follow the same power-law. **Figure 6J** demonstrates this point: both interictal events and delivered pulses fit within the same power-law relationship of the reference population (from[15]); in fact, their CV was not significantly different from what estimated from the μ vs CV fitting parameters (empirical CV: 0.35 ± 0.05, estimated CV: 0.41 ± 0.07; $p > 0.05$, Welch test). Thus, the bridge robustness to failure may reside in the preserved temporal statistics of the relayed interictal events.

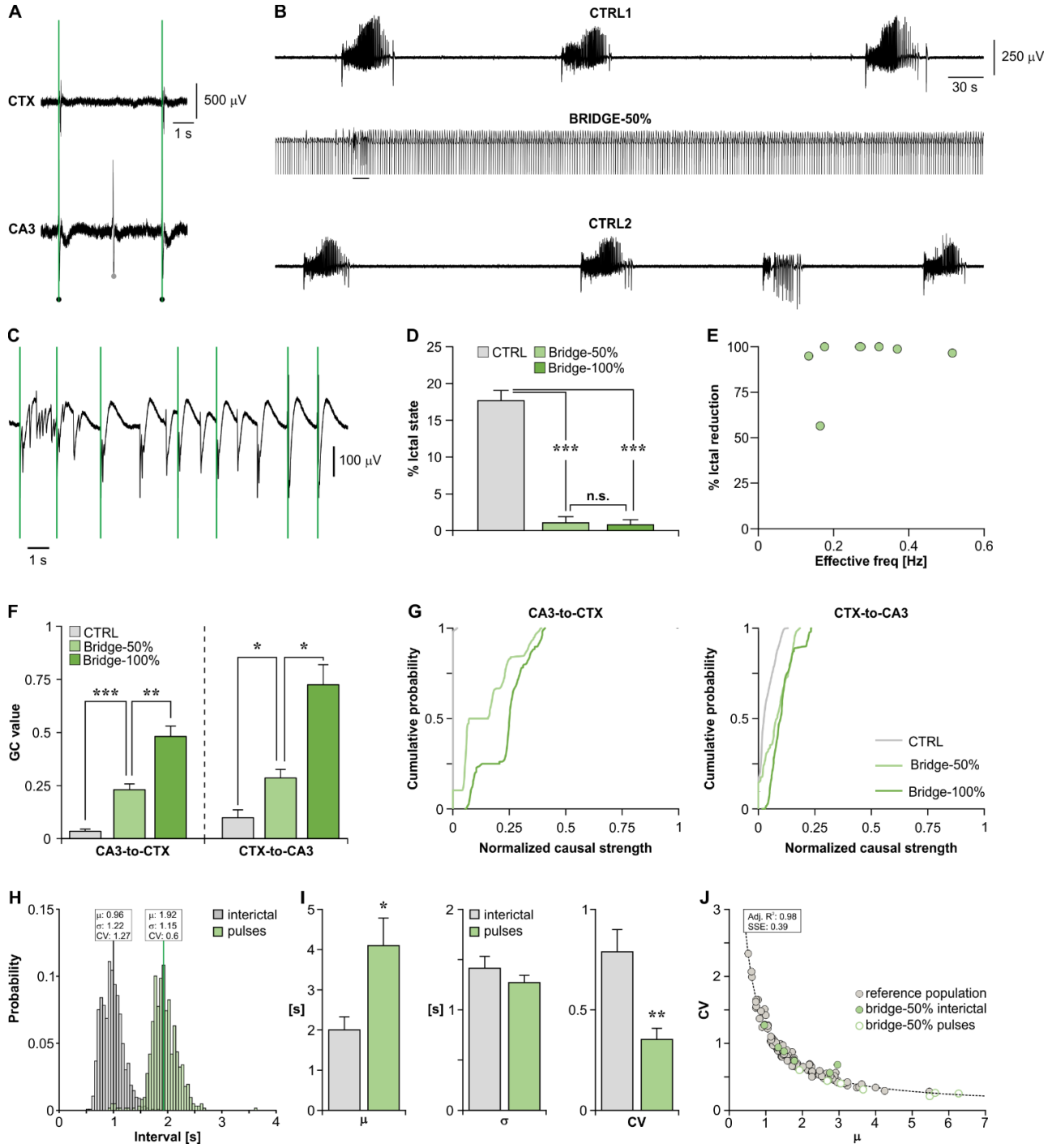

Figure 6 – Bridge robustness to failure suggests a pulse-timing and pattern dependent efficacy.

*A. Representative recordings from CTX and CA3 illustrating the operating mode of the bridge-50%. The black dots indicate the detected interictal events that triggered the stimulation, while the grey dot indicates the detected interictal event that did not trigger it. The vertical green bars mark the pulse timings. B. Recording from the CTX during a representative experiment: the bridge abolished full-blown ictal activity and the only anomalous event was a short population burst (solid line), eventually entrained by the stimulation. C. Anomalous population burst indicated by the solid line in B, visualized at expanded time scale. Vertical green bars mark the pulse timings. D. Summary of the results statistics obtained from this dataset (n = 7 brain slices) demonstrating the similar performance of the bridge-50% and the bridge-100%. E. The efficacy of the bridge-50% does not correlate with its effective stimulation frequency (n. pulses/stimulation duration). F,G. Granger causality (F) and OPTN (G) reveal the partial restoration of the functional connectivity of the hippocampal loop in both directions, compared to the bridge-100%. H. Distributions of the interictal and inter-pulse intervals for the experiment in B show that the inter-pulse distribution is right-shifted compared to the interictal distribution, while the shape is preserved. I. Comparison of the distribution parameters m, s and CV between interictal and pulse intervals: in the latter, the m parameter is ~double and accounts for the ~halved CV. J. The □ vs CV relationship of the inter-pulse intervals of the bridge-50% fits the distribution of the original interictal events and of a larger interictal population of reference (n = 105 brain slices, same dataset as in[15]), indicating that the inter-pulse intervals represent a subset of the same population. * p < 0.05; ** p < 0.01; *** p < 0.001.*

To corroborate this point, the counter-proof would be a scenario resembling the unreliable operation of the DBS device; namely, failure should be designed to dissipate the original interictal temporal dynamics and yield a variable failure rate throughout the experiment, rather than be time-bound to the *nth* interictal event. Here, we set a blanking window of 5 s during which the event detection would not trigger the stimulator, hence the failure rate would depend on the number of interictal discharges occurring during the set time constraint. This paradigm is hereafter referred to as bridge-bw5. The duration of the blanking window reflected two observations: **(i)** the bridge-50% outperformed the limit open-loop stimulation frequency of 0.2 Hz (*cf.* **Figure 6D**); **(ii)** the μ vs CV power-law relationship of interictal events tends to its asymptote at μ >= 5 s, i.e., 0.2 Hz (*cf.* **Figure 6I**); herein, the CV reaches its lowest values tending toward a periodic pattern.

As shown in **Figure 7A**, this paradigm indeed yielded a variable pulse-to-pulse failure, which overall ranged between 72.73 and 84.64% (79.32 ± 1.32%; n = 6 brain slices). In this series of experiments, again, the bridge-100% was used as positive control and the stimulation protocols were shuffled.

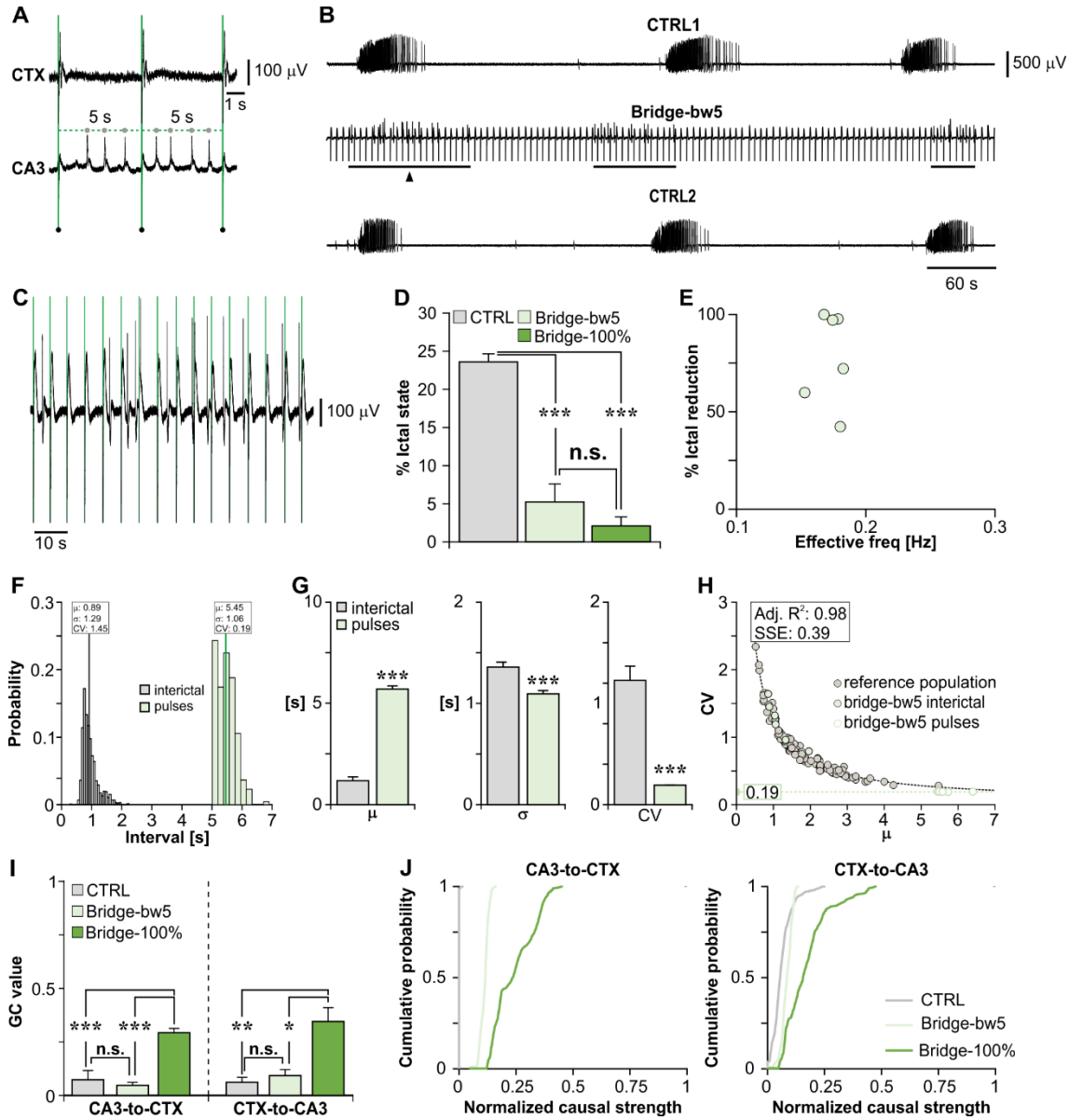

Figure 7 – The bridge performs unreliably upon dissipation of interictal temporal statistics in the pulse timing.
A. Representative recordings from CTX and CA3 illustrating the operating mode of the bridge-bw5. The black dots indicate the detected interictal events that triggered the stimulation, while the grey dots indicate the detected events that fall within the 5-s blanking window. The vertical green bars mark the pulse timings. B. Recording from the CTX during a representative best-case experiment: the bridge abolished full-blown ictal activity and the only anomalous events were stimulation-independent interictal-like discharges (solid lines). C. Representative case of anomalous stimulus-independent activity corresponding to the

*epoch pointed by the arrowhead in B, visualized at expanded time scale. The vertical green bars mark the pulse timings. D. Summary of the results statistics obtained from this dataset (n = 6 brain slices) showing a statistically similar efficacy of the bridge-bw5 and the bridge-100%. E. The efficacy of the bridge-bw5 is highly variable and does not correlate with its effective stimulation frequency (n. pulses/stimulation duration). F. Distributions of the interictal and inter-pulse intervals for the experiment in B: the inter-pulse distribution is right-shifted and its shape is unpreserved compared to the interictal distribution. G. Each of the distribution parameters m, s and CV are different between interictal and pulse intervals. H. The μ vs CV relationship of the interictal IEI falls within the reference distribution (n = 105 brain slices, same dataset as in [15]); however, the inter-pulse intervals of the bridge-bw5 fall below the asymptote of the reference fitted curve, indicating that they do not represent a subset of the same population. The CV values approximate a constant of 0.19 (dashed line), which is in contrast with the inter-individual variability observed in interictal patterns. I. Granger causality confirms the poor performance of the bridge-bw5 in re-establishing the functional connectivity of the hippocampal loop, which does not differ from CTRL. (J) OPTN reveals a weak restoration of the CA3-to-CTX functional connectivity, reflecting the misalignment of the bridge with the temporal dynamics of the CA3-CTX interplay. * p < 0.05; ** p < 0.01; *** p < 0.001.*

Figure 7B shows a representative best-case scenario in which the bridge-bw5 prevented ictal activity; cortical networks were fully entrained by the stimulation and only generated short epochs of stimulus-independent interictal-like events (solid lines; epoch marked by the arrowhead is expanded in **Figure 7C**). As summarized in **Figure 7D**, statistical analysis indicated that the bridge-bw5 overall performed similarly to the bridge-100% (ictal state % – pooled CTRLs: 23.61 ± 1.04, bridge-bw5: 5.25 ± 2.36, bridge-100%: 2.1 ± 1.19; ictal state reduction vs preceding CTRL – bridge-bw5: 77.59 ± 10.73%; bridge-100%: 90.33 ± 6.32; one-way ANOVA, F(df): 79.9(2), $p < 0.001$ for both bridges against the pooled CTRLs; $p > 0.05$ between the two bridges). However, its performance was highly variable, ranging 44.63-100% of ictal reduction, and achieving full efficacy in only 50% of the cases (**Figure 7E**). The variability in ictal state reduction is consistent with the misalignment of the bridge with the temporal evolution of the CA3-CTX dynamic interplay as a consequence of the constrained inter-pulse interval. In keeping with this, not only the distribution of the inter-pulse intervals was right shifted compared to the original interictal IEI distribution; its shape did not seem preserved (**Figure 7F**; data from representative case in panel **B**). Comparison of the μ, σ, and CV parameters of pulse versus interictal intervals in the whole dataset confirmed the significant change in each of them (**Figure 7G**; μ – interictal: 1.19 ± 0.18, pulses 5.7 ± 0.16, $p < 0.001$; σ – interictal: 1.36 ± 0.05, pulses 1.09 ± 0.03, $p < 0.001$; CV – interictal: 1.23 ± 0.14, pulses: 0.19 ± 0.001, $p < 0.001$, Welch test). Further, as shown in **Figure 7H**, the μ vs CV relationship of delivered pulses fell below the asymptote of the reference curve; remarkably, the CV parameter approximated a constant value (0.19 ± 0.001) which differed significantly from what estimated from the fitting parameters of the reference curve (0.27 ± 0.006, $p < 0.001$, Welch test). Thus, constraining the bridge to a minimum inter-pulse interval dissipates the statistical properties of the interictal pattern of reference, and yields a stimulation policy that approximates periodic pacing. In keeping with this, the bridge-bw5 behaved similarly to what reported for fixed-frequency stimulation at 0.2 Hz[14, 66], exhibiting a likewise poor and variable efficacy. Further, Granger causality evidenced no significant change in the CA3-CTX correlation in both directions of the loop (**Figure 7I**; GC value CA3-to-CTX – CTRL: 0.07 ± 0.04, bridge-bw5: 0.05 ± 0.01, bridge-100%: 0.29 ± 0.02; ANOVA F(df): 34.1(2), bridge-bw5 vs CTRL: $p > 0.05$, bridge-bw5 vs bridge-100%: $p < 0.001$, bridge-100% vs CTRL: $p < 0.001$. GC value CTX-to-CA3 – CTRL: 0.06 ± 0.02, bridge-bw5: 0.09 ± 0.03, bridge-100%: 0.35 ± 0.07; ANOVA F(df): 16.5(2); bridge-bw5 vs CTRL: $p > 0.05$, bridge-bw5 vs bridge-100%: $p < 0.05$, bridge-100% vs CTRL: $p < 0.01$); likewise, OPTN unveiled only a weak causal strength in the CA3-to-CTX direction (**Figure 7J**; see **supplementary Table 3** for detailed statistics). Taken together, these results reflect the unreliable CA3-driven stimulation: while they corroborate that the bridge effectiveness and robustness stem in mirroring the CA3-CTX dynamic interplay, they further emphasize the crucial importance of the reliable operation of DBS devices and of grounding DBS policies in meaningful brain patterns.

Figure 8 provides the performance overview for the different bridging paradigms, including ictal reduction percentage (**A**), and the achieved functional restoration of the hippocampal loop compared to connected/disconnected brain slices, taken as positive and negative control, respectively (**B-C**). The GC values (**B**) show a clear trend toward increased functional connectivity with the increased bridge efficiency (see **Supplementary Table 4** for full results statistics). OPTN-based causality measures (**C**) show a similar trend, although they highlight a partial restoration of the CA3-to-CTX causal strength in the bridge-bw5, which is similar to the bridge-50% (see **Supplementary Table 5** for detailed statistics).

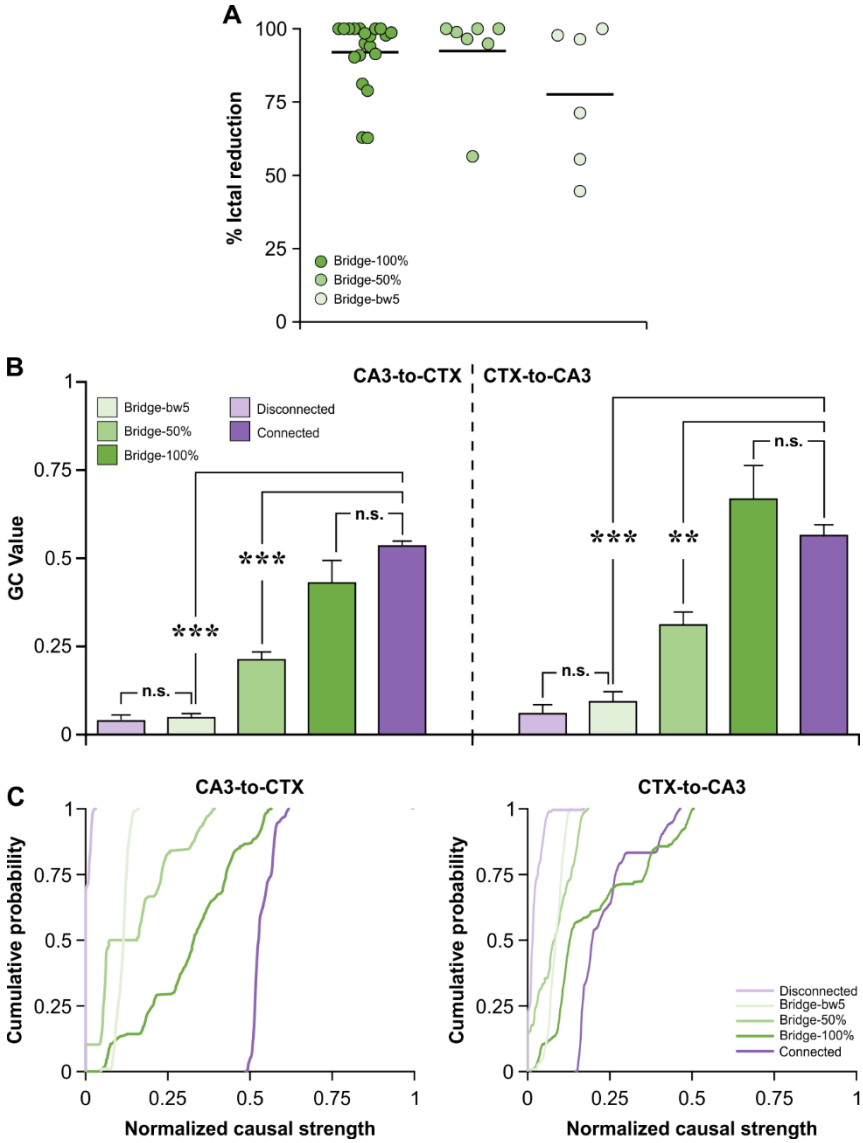

Figure 8 – Performance overview of the bridge under different failure testing paradigms.
A. Direct comparison of ictal state reduction achieved by the three bridge paradigms. Each dot represents one experiment, while the solid line indicates the mean % of ictal reduction for each dataset. B, C. Comparison of the restoration of functional connectivity in the three bridging paradigms vs disconnected and connected brain slices, using Granger causality (B) and OPTN (C).

Discussion

In this work, we have devised an interictal-driven closed-loop stimulation to bridge hippocampus and CTX and control limbic seizures. We have shown that **(i)** the bridge is feasible and effective in controlling ictal activity; **(ii)** it restores the functional connectivity of the hippocampal loop; **(iii)** its efficacy and robustness stem in mirroring the adaptive properties of the CA3, which acts as biological neuromodulator.

The hippocampal subfield CA3 has been widely studied for its pacemaker-like properties [63, 64] and its anti-ictogenic function in limbic circuits involved in MTLE [12, 60-62]. Here, we provide the first evidence that the CA3 acts as adaptive biological neuromodulator of cortical hyperexcitability; namely, cortical ictal activity invading the hippocampus proper drive the CA3, which responds with accelerations of interictal events aimed at halting the seizure. By relaying the adaptive behavior of the CA3 back to the CTX, the bridge effectively controls cortical ictal activity. The inherent mirroring feature of the bridge makes it robust to failure when the intervals of the delivered pulses reflect the temporal evolution of the CA3-CTX dynamic

interplay; while the CA3 adapts to cortical inputs, interictal-driven evoked responses in the CTX will ensue a process of dynamic reciprocal adaptation of the two structures. In keeping with this, the bridge demonstrated robust to 50% failure, primarily mimicking the CA3 functional impairment possibly accompanying MTLE [43]; at variance, dissipating the CA3 interictal temporal dynamics, primarily mimicking hardware malfunction, yielded an unreliable bridge performance. Thus, the artificial re-establishment of the functional connectivity in the CA3-to-CTX direction ensues a process of dynamic adaptation of the CA3-CTX system aiding it in settling to a non-seizing equilibrium. In a broader perspective, these results also indicate that the bridge may be robust to the functional impairment of the CA3 that is often observed in MTLE patients with hippocampal sclerosis. Along with the crucial importance of DBS devices reliability, these results further emphasize the need of grounding DBS policies in meaningful brain patterns.

Interictal discharges present the key for an effective closed-loop DBS as they reflect the propensity of the epileptic brain to generate seizures [10, 11, 67]. Nonetheless, their direct exploitation in closed-loop DBS has never been considered; this is because a clear definition of their pro-ictogenic versus anti-ictogenic role is still a matter of debate due to the general assumption that the two roles are mutually exclusive. In contrast, emerging evidence strongly indicates that such dichotomic definition is invalid; rather, it points to the co-existence of these opposite roles as state-dependent features in the bistable dynamical system that is the epileptic brain [10, 11, 67, 68]. In this view, interictal discharges may be exploited to probe ongoing brain dynamics (seizure prediction) as well as for neuromodulation (seizure prevention), thus overcoming the need of complex seizure prediction/detection algorithms as well as delayed stimulation and a trial-and-error approach. Along these lines, in the present work, the CA3-driven interictal activity could be deployed as a biological probe of ongoing cortical dynamics as well as anti-ictogenic neuromodulator. With this, our work demonstrates the possibility of deploying endogenous interictal patterns to reliably drive closed-loop DBS for epilepsy treatment. Specifically, the biohybrid approach proposed here provides the proof-of-concept for two distinct yet complementary aspects for biomedical devices for epilepsy treatment: **(i)** a bridging neuroprosthesis reconnecting brain areas whose impaired functional dialogue leads to seizure generation (here, the CA3 and the parahippocampal CTX), and **(ii)** an interictal-based grammar for closed-loop DBS.

Outlook

Closed-loop DBS is the latest frontier in neuromodulation to ameliorate drug-refractory epilepsy, as it provides ad hoc intervention based on the patient's brain activity. However, it is still far from offering a seizure-free life due to our limited understanding of the dynamical unfolding of epilepsy. As a result, it entails a trial-and-error approach based on arbitrary settings, and it is primarily designed to halt rather than prevent seizures. The lack of a unifying framework in DBS highlights the need of pinpointing the most appropriate timing of stimulation and rooting pulse sequences in physiologically meaningful features with the ultimate goal of offering a seizure-free life, rather than seizure reduction. By demonstrating this principle, our work paves the way to an interictal-based grammar for closed-loop DBS as well as for a bridging neuroprosthesis to treat epilepsy.

References

[1] Nagaraj V, Lee ST, Krook-Magnuson E, Soltesz I, Benquet P, Irazoqui PP, et al. Future of Seizure Prediction and Intervention: Closing the Loop. Journal of Clinical Neurophysiology. 2015;32(3).
[2] Wagenaar DA, Madhavan R, Pine J, Potter SM. Controlling bursting in cortical cultures with closed-loop multi-electrode stimulation. J Neurosci. 2005;25(3):680-8.
[3] Ben-Menachem E, Krauss GL. Epilepsy: responsive neurostimulation-modulating the epileptic brain. Nature reviews Neurology. 2014;10(5):247-8.
[4] Morrell MJ, Halpern C. Responsive Direct Brain Stimulation for Epilepsy. Neurosurgery clinics of North America. 2016;27(1):111-21.
[5] Pineau J, Guez A, Vincent R, Panuccio G, Avoli M. Treating epilepsy via adaptive neurostimulation: a reinforcement learning approach. Int J Neural Syst. 2009;19(4):227-40.
[6] Panuccio G, Guez A, Vincent R, Avoli M, Pineau J. Adaptive control of epileptiform excitability in an in vitro model of limbic seizures. Experimental neurology. 2013;241:179-83.
[7] Kuhlmann L, Lehnertz K, Richardson MP, Schelter B, Zaveri HP. Seizure prediction — ready for a new era. Nature Reviews Neurology. 2018;14(10):618-30.
[8] Sandler RA, Song D, Hampson RE, Deadwyler SA, Berger TW, Marmarelis VZ. Hippocampal closed-loop modeling and implications for seizure stimulation design. Journal of Neural Engineering. 2015;12(5):056017.
[9] Geller EB, Skarpaas TL, Gross RE, Goodman RR, Barkley GL, Bazil CW, et al. Brain-responsive neurostimulation in patients with medically intractable mesial temporal lobe epilepsy. Epilepsia. 2017;58(6):994-1004.
[10] Dzhala VI, Staley KJ. Transition from Interictal to Ictal Activity in Limbic Networks In Vitro. The Journal of Neuroscience. 2003;23(21):7873-80.
[11] Staley KJ, Dudek FE. Interictal spikes and epileptogenesis. Epilepsy Curr. 2006;6(6):199-202.
[12] Barbarosie M, Avoli M. CA3-driven hippocampal-entorhinal loop controls rather than sustains in vitro limbic seizures. J Neurosci. 1997;17(23):9308-14.
[13] Blümcke I, Thom M, Aronica E, Armstrong DD, Bartolomei F, Bernasconi A, et al. International consensus classification of hippocampal sclerosis in temporal lobe epilepsy: A Task Force report from the ILAE Commission on Diagnostic Methods. Epilepsia. 2013;54(7):1315-29.
[14] D'Arcangelo G, Panuccio G, Tancredi V, Avoli M. Repetitive low-frequency stimulation reduces epileptiform synchronization in limbic neuronal networks. Neurobiol Dis. 2005;19(1-2):119-28.
[15] Caron D, Canal-Alonso A, Panuccio G. Mimicking CA3 Temporal Dynamics Controls Limbic Ictogenesis. Biology. 2022;11(3).
[16] Zhang SH, Sun HL, Fang Q, Zhong K, Wu DC, Wang S, et al. Low-frequency stimulation of the hippocampal CA3 subfield is anti-epileptogenic and anti-ictogenic in rat amygdaloid kindling model of epilepsy. Neuroscience letters. 2009;455(1):51-5.
[17] Wyckhuys T, Boon P, Raedt R, Van Nieuwenhuyse B, Vonck K, Wadman W. Suppression of hippocampal epileptic seizures in the kainate rat by Poisson distributed stimulation. Epilepsia. 2010;51(11):2297-304.
[18] Wyckhuys T, Raedt R, Vonck K, Wadman W, Boon P. Comparison of hippocampal Deep Brain Stimulation with high (130Hz) and low frequency (5Hz) on afterdischarges in kindled rats. Epilepsy research. 2010;88(2-3):239-46.
[19] Rashid S, Pho G, Czigler M, Werz MA, Durand DM. Low frequency stimulation of ventral hippocampal commissures reduces seizures in a rat model of chronic temporal lobe epilepsy. Epilepsia. 2012;53(1):147-56.
[20] Van Nieuwenhuyse B, Raedt R, Delbeke J, Wadman WJ, Boon P, Vonck K. In search of optimal DBS paradigms to treat epilepsy: bilateral versus unilateral hippocampal stimulation in a rat model for temporal lobe epilepsy. Brain stimulation. 2015;8(2):192-9.
[21] Chen N, Gao Y, Yan N, Liu C, Zhang JG, Xing WM, et al. High-frequency stimulation of the hippocampus protects against seizure activity and hippocampal neuronal apoptosis induced by kainic acid administration in macaques. Neuroscience. 2014;256:370-8.
[22] Paschen E, Elgueta C, Heining K, Vieira DM, Kleis P, Orcinha C, et al. Hippocampal low-frequency stimulation prevents seizure generation in a mouse model of mesial temporal lobe epilepsy. Elife. 2020;9.
[23] Zhong K, Wu D-C, Jin M-M, Xu Z-H, Wang Y, Hou W-W, et al. Wide therapeutic time-window of low-frequency stimulation at the subiculum for temporal lobe epilepsy treatment in rats. Neurobiology of Disease. 2012;48(1):20-6.
[24] Sprengers M, Raedt R, Larsen LE, Delbeke J, Wadman WJ, Boon P, et al. Deep brain stimulation reduces evoked potentials with a dual time course in freely moving rats: Potential neurophysiological basis for intermittent as an alternative to continuous stimulation. Epilepsia. 2020;61(5):903-13.

[25] Cukiert A, Cukiert CM, Burattini JA, Mariani PP, Bezerra DF. Seizure outcome after hippocampal deep brain stimulation in patients with refractory temporal lobe epilepsy: A prospective, controlled, randomized, double-blind study. Epilepsia. 2017;58(10):1728-33.
[26] Velasco M, Velasco F, Velasco AL, Boleaga B, Jimenez F, Brito F, et al. Subacute Electrical Stimulation of the Hippocampus Blocks Intractable Temporal Lobe Seizures and Paroxysmal EEG Activities. Epilepsia. 2000;41(2):158-69.
[27] Vonck K, Boon P, Achten E, De Reuck J, Caemaert J. Long-term amygdalohippocampal stimulation for refractory temporal lobe epilepsy. Annals of Neurology. 2002;52(5):556-65.
[28] Tellez-Zenteno JF, McLachlan RS, Parrent A, Kubu CS, Wiebe S. Hippocampal electrical stimulation in mesial temporal lobe epilepsy. Neurology. 2006;66(10):1490.
[29] Boon P, Vonck K, De Herdt V, Van Dycke A, Goethals M, Goossens L, et al. Deep Brain Stimulation in Patients with Refractory Temporal Lobe Epilepsy. Epilepsia. 2007;48(8):1551-60.
[30] McLachlan RS, Pigott S, Tellez-Zenteno JF, Wiebe S, Parrent A. Bilateral hippocampal stimulation for intractable temporal lobe epilepsy: Impact on seizures and memory. Epilepsia. 2010;51(2):304-7.
[31] Boëx C, Seeck M, Vulliémoz S, Rossetti AO, Staedler C, Spinelli L, et al. Chronic deep brain stimulation in mesial temporal lobe epilepsy. Seizure - European Journal of Epilepsy. 2011;20(6):485-90.
[32] Bondallaz P, Boëx C, Rossetti AO, Foletti G, Spinelli L, Vulliemoz S, et al. Electrode location and clinical outcome in hippocampal electrical stimulation for mesial temporal lobe epilepsy. Seizure. 2013;22(5):390-5.
[33] Jin H, Li W, Dong C, Wu J, Zhao W, Zhao Z, et al. Hippocampal deep brain stimulation in nonlesional refractory mesial temporal lobe epilepsy. Seizure - European Journal of Epilepsy. 2016;37:1-7.
[34] Boon PAJM. Hippocampal deep brain stimulation for epilepsy. Brain Stimulation: Basic, Translational, and Clinical Research in Neuromodulation. 2017;10(2):431-2.
[35] Bartoli A, Tyrand R, Vargas MI, Momjian S, Boëx C. Low Frequency Microstimulation Is Locally Excitatory in Patients With Epilepsy. Frontiers in neural circuits. 2018;12(22).
[36] Fisher PD, Sperber EF, Moshe SL. Hippocampal sclerosis revisited. Brain & development. 1998;20(8):563-73.
[37] Wozny C, Kivi A, Lehmann T-N, Dehnicke C, Heinemann U, Behr J. Comment on "On the Origin of Interictal Activity in Human Temporal Lobe Epilepsy in Vitro". Science. 2003;301(5632):463.
[38] Knopp A, Kivi A, Wozny C, Heinemann U, Behr J. Cellular and network properties of the subiculum in the pilocarpine model of temporal lobe epilepsy. Journal of Comparative Neurology. 2005;483(4):476-88.
[39] Velasco AL, Saucedo-Alvarado PE, Alejandre-Sánchez M, Guzmán-Jiménez DE, González-Garcia I, Velasco F. New Horizons in Temporal Lobe Seizure Control. Journal of Clinical Neurophysiology. 2021;38(6):478-84.
[40] Benini R, Avoli M. Rat subicular networks gate hippocampal output activity in an in vitro model of limbic seizures. J Physiol. 2005;566(Pt 3):885-900.
[41] Cohen I, Navarro V, Clemenceau S, Baulac M, Miles R. On the origin of interictal activity in human temporal lobe epilepsy in vitro. Science. 2002;298(5597):1418-21.
[42] de Guzman P, Inaba Y, Biagini G, Baldelli E, Mollinari C, Merlo D, et al. Subiculum network excitability is increased in a rodent model of temporal lobe epilepsy. Hippocampus. 2006;16(10):843-60.
[43] Panuccio G, D'Antuono M, de Guzman P, De Lannoy L, Biagini G, Avoli M. In vitro ictogenesis and parahippocampal networks in a rodent model of temporal lobe epilepsy. Neurobiol Dis. 2010;39(3):372-80.
[44] Panuccio G, Colombi I, Chiappalone M. Recording and Modulation of Epileptiform Activity in Rodent Brain Slices Coupled to Microelectrode Arrays. J Vis Exp. 2018(135).
[45] Rutecki PA, Lebeda FJ, Johnston D. 4-Aminopyridine produces epileptiform activity in hippocampus and enhances synaptic excitation and inhibition. J Neurophysiol. 1987;57(6):1911-24.
[46] Daubechies I. Ten lectures on wavelets: Society for Industrial and Applied Mathematics; 1992. 357 p.
[47] Toprani S, Durand DM. Fiber tract stimulation can reduce epileptiform activity in an in-vitro bilateral hippocampal slice preparation. Experimental neurology. 2013;240:28-43.
[48] Mizuseki K, Buzsaki G. Preconfigured, skewed distribution of firing rates in the hippocampus and entorhinal cortex. Cell reports. 2013;4(5):1010-21.
[49] Buzsaki G, Mizuseki K. The log-dynamic brain: how skewed distributions affect network operations. Nature reviews Neuroscience. 2014;15(4):264-78.
[50] Ruan Y, Donner RV, Guan S, Zou Y. Ordinal partition transition network based complexity measures for inferring coupling direction and delay from time series. Chaos. 2019;29(4):043111.
[51] Subramaniyam NP, Donner RV, Caron D, Panuccio G, Hyttinen J. Causal coupling inference from multivariate time series based on ordinal partition transition networks. Nonlinear Dynamics. 2021;105(1):555-78.
[52] Takens F, editor Detecting strange attractors in turbulence. Dynamical Systems and Turbulence, Warwick 1980; 1981 1981//; Berlin, Heidelberg: Springer Berlin Heidelberg.
[53] Kantz H, Schreiber T. Nonlinear Time Series Analysis. 2 ed. Cambridge: Cambridge University Press; 2003.

[54] Puthanmadam Subramaniyam N, Hyttinen J. Characterization of dynamical systems under noise using recurrence networks: Application to simulated and EEG data. Physics Letters A. 2014;378(46):3464-74.
[55] Knijnenburg TA, Wessels LFA, Reinders MJT, Shmulevich I. Fewer permutations, more accurate P-values. Bioinformatics. 2009;25(12):i161-i8.
[56] Hintze JL, Nelson RD. Violin Plots: A Box Plot-Density Trace Synergism. The American Statistician. 1998;52(2):181-4.
[57] Sohal VS, Sun FT. Responsive Neurostimulation Suppresses Synchronized Cortical Rhythms in Patients with Epilepsy. Neurosurgery clinics of North America. 2011;22(4):481-8.
[58] Ronborg SN, Esteller R, Tcheng TK, Greene DA, Morrell MJ, Wesenberg Kjaer T, et al. Acute effects of brain-responsive neurostimulation in drug-resistant partial onset epilepsy. Clin Neurophysiol. 2021;132(6):1209-20.
[59] Seth AK, Barrett AB, Barnett L. Granger causality analysis in neuroscience and neuroimaging. J Neurosci. 2015;35(8):3293-7.
[60] Swartzwelder HS, Lewis DV, Anderson WW, Wilson WA. Seizure-like events in brain slices: suppression by interictal activity. Brain Res. 1987;410(2):362-6.
[61] Bragdon AC, Kojima H, Wilson WA. Suppression of interictal bursting in hippocampus unleashes seizures in entorhinal cortex: a proepileptic effect of lowering [K+]o and raising [Ca2+]o. Brain Res. 1992;590(1-2):128-35.
[62] Barbarosie M, Louvel J, Kurcewicz I, Avoli M. CA3-released entorhinal seizures disclose dentate gyrus epileptogenicity and unmask a temporoammonic pathway. J Neurophysiol. 2000;83(3):1115-24.
[63] Colom LV, Saggau P. Spontaneous interictal-like activity originates in multiple areas of the CA2-CA3 region of hippocampal slices. J Neurophysiol. 1994;71(4):1574-85.
[64] Wittner L, Miles R. Factors defining a pacemaker region for synchrony in the hippocampus. J Physiol. 2007;584(Pt 3):867-83.
[65] Shils JL, Alterman RL, Arle JE. Deep Brain Stimulation Fault Testing. In: Tarsy D, Vitek JL, Starr PA, Okun MS, editors. Deep Brain Stimulation in Neurological and Psychiatric Disorders. Totowa, NJ: Humana Press; 2008. p. 473-94.
[66] Bush K, Panuccio G, Avoli M, Pineau J. Evidence-based modeling of network discharge dynamics during periodic pacing to control epileptiform activity. J Neurosci Methods. 2012;204(2):318-25.
[67] Chang WC, Kudlacek J, Hlinka J, Chvojka J, Hadrava M, Kumpost V, et al. Loss of neuronal network resilience precedes seizures and determines the ictogenic nature of interictal synaptic perturbations. Nat Neurosci. 2018;21(12):1742-52.
[68] Chvojka J, Kudlacek J, Chang WC, Novak O, Tomaska F, Otahal J, et al. The role of interictal discharges in ictogenesis - A dynamical perspective. Epilepsy Behav. 2021;121(Pt B):106591.

Supplementary

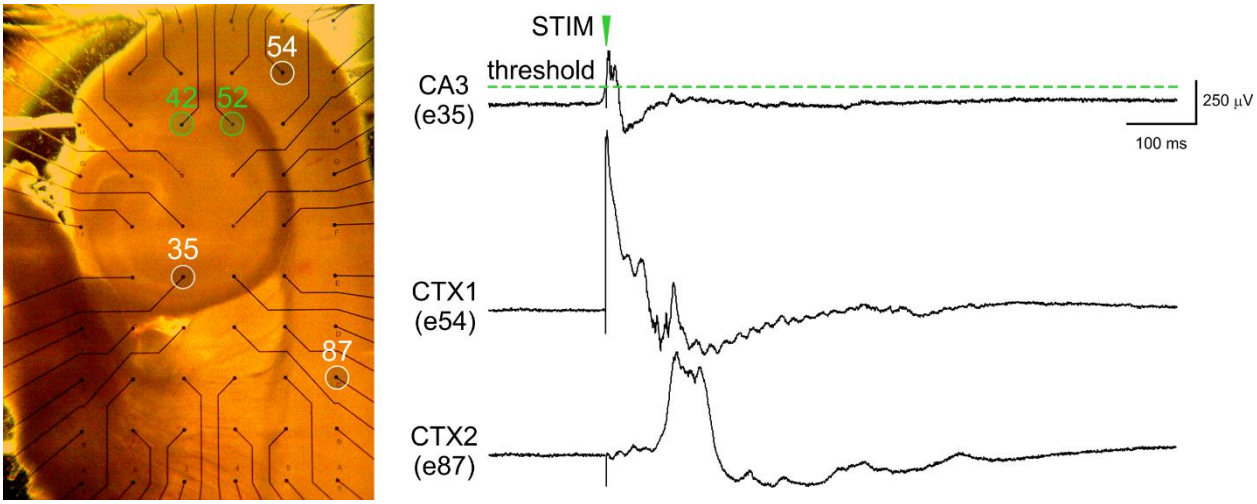

Supplementary Figure 1 – Operation of the closed-loop biohybrid bridging.

On the left is the picture of a hippocampus-CTX slice coupled to a planar MEA, where the white and green circles indicate the recording and stimulating electrodes, respectively. On the right are representative events from the CA3 (feedback signal) and the CTX (evoked responses). The threshold value for event detection is set at approximately one half of the signal amplitude (dashed green line). Upon threshold crossing, a pulse is delivered to the subiculum through the stimulating electrode pair, in turn evoking responses in the CTX. Stimulus artifacts are clipped for clarity, and the pulse time is indicated by the green downward arrow.

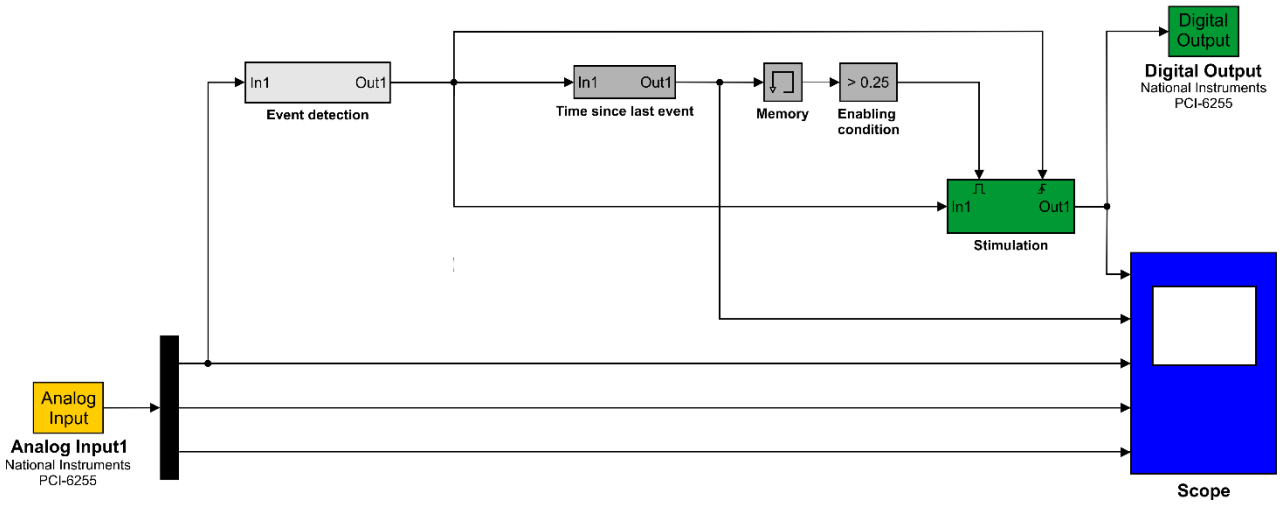

Supplementary Figure 2 – Simulink model for biohybrid bridging.

The model consists of input (yellow), processing (grey) and output (green) blocks, along with a scope window (blue). The processing blocks include routines for the event detection (light grey) and the decision to stimulate (dark grey). The Analog Input block retrieves the signals from the MEA system and feeds the signal of one selected electrode from the CA3 to the Event detection block. The latter implements a hard-threshold crossing algorithm and feeds its output to the Time since last event block to start the decision routine. The Stimulation block is triggered if the enabling condition is met. The stimulation block then triggers the Digital Output block, which, in turn, activates the TTL signal to the external stimulator. The Scope window enables the real-time visualization of the MEA signals, as well as the output of the *Event detection*, *Time since last event*, and *Stimulation* blocks.

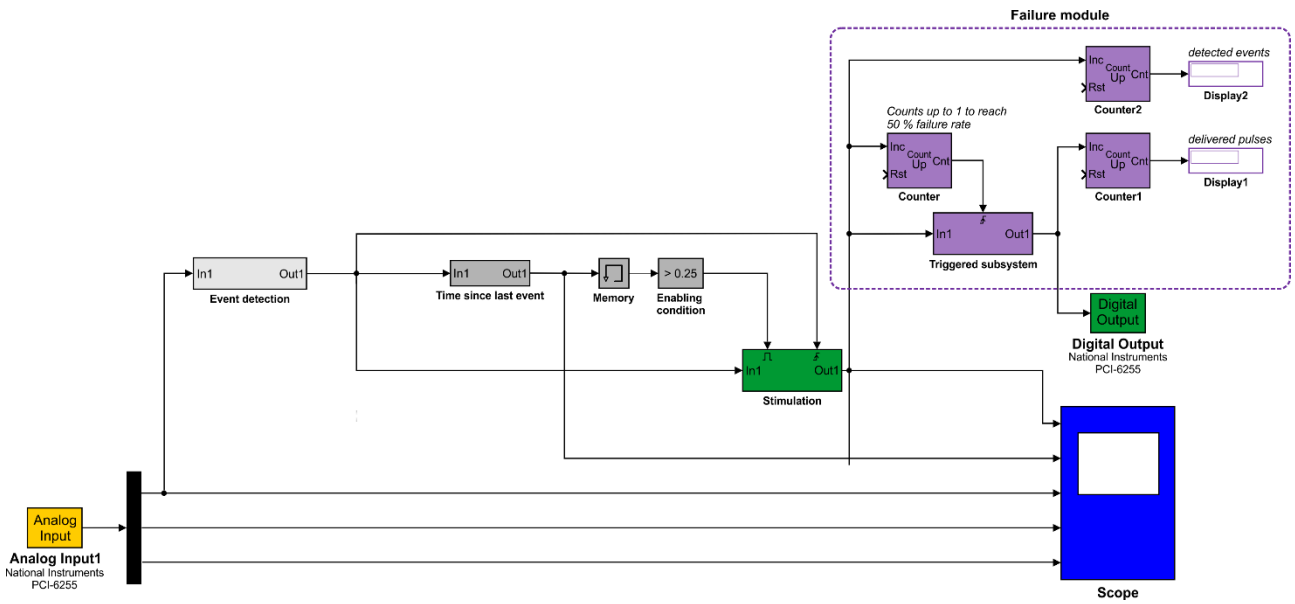

Supplementary Figure 3 – Simulink model implementation for 50% failure testing.

The model is based on the same architecture depicted in **Supplementary Figure 3** with the addition of a failure module (purple blocks, framed by the purple dashed box), based on a counter of triggered events.

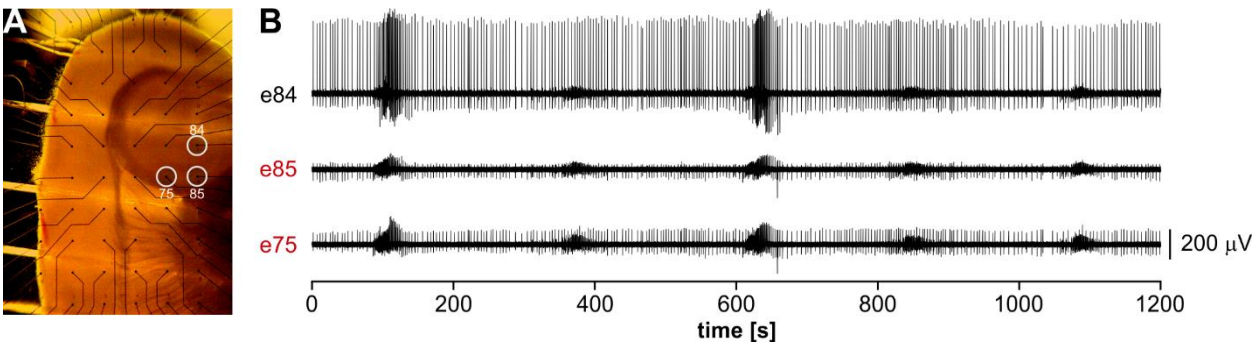

Supplementary Figure 4 – Choice of the optimal feedback electrode.

A. Picture of a hippocampus-CTX slice placed on a 6x10 MEA, showing the set of choices for the CA3 feedback electrode. **B.** Recordings from the electrodes indicated in **A** illustrating optimal (black electrode) and sub-optimal (red electrodes) signal features. In the latter, the signal-to-noise ratio is low and the amplitude of ictal discharges masks the interictal events. The optimal feedback electrode in this representative case is e84 because of the high signal-to-noise ratio and the very small difference in amplitude of ictal discharges compared to the interictal events.

Supplementary Table 1 – Pairwise statistical comparison of the bridge performance, assessed with OPTN: W_1 distance (data from Figure 2E).

CA3-to-CTX	CTRL1	Bridge	CTRL2
CTRL1		0.31***	0
Bridge	0.31***		0.31***
CTRL2	0	0.31***	

CTX-to-CA3	CTRL1	Bridge	CTRL2
CTRL1		0.12***	0.02***
Bridge	0.12***		0.14***
CTRL2	0.02***	0.14***	

*** $p < 0.001$.

Table 2 – Pairwise statistical comparison of the bridge-50% performance, assessed with OPTN: W_1 distance (data from Figure 6G).

CA3-to-CTX	CTRL (pooled)	Bridge-50%	Bridge-100%
CTRL (pooled)		0.14***	0.23***
Bridge-50%	0.14***		0.09***
Bridge-100%	0.23***	0.09***	

CTX-to-CA3	CTRL (pooled)	Bridge-50%	Bridge-100%
CTRL (pooled)		0.04***	0.06***
Bridge-50%	0.04***		0.02***
Bridge-100%	0.06***	0.02***	

*** $p < 0.001$.

Table 3 – Pairwise statistical comparison of the bridge-bw5 performance, assessed with OPTN: W_1 distance (data from Figure 6G).

CA3-to-CTX	CTRL (pooled)	Bridge-bw5	Bridge-100%
CTRL (pooled)		0.1***	0.24***
Bridge-bw5	0.1***		0.13***
Bridge-100%	0.24***	0.13***	

CTX-to-CA3	CTRL (pooled)	Bridge-bw5	Bridge-100%
CTRL (pooled)		0.02***	0.1***
Bridge-bw5	0.02***		0.08***
Bridge-100%	0.1***	0.08***	

*** $p < 0.001$.

Supplementary Table 4 – Bridge performance overview, assessed with Granger causality (data from Figure 8B).

CA3-to-CTX	Disconnected	Bridge-bw5	Bridge-50%	Bridge-100%	Connected
Disconnected		n.s.	***	***	***
Bridge-bw5	n.s.		**	**	***
Bridge-50%	**	**		*	***
Bridge-100%	**	**	*		n.s.
Connected	***	***	***	n.s.	

CTX-to-CA3	Disconnected	Bridge-bw5	Bridge-50%	Bridge-100%	Connected
Disconnected		n.s.	***	***	***
Bridge-bw5	n.s.		**	**	***
Bridge-50%	***	**		*	**
Bridge-100%	***	**	*		n.s.
Connected	***	***	**	n.s.	

* $p < 0.05$; ** $p < 0.01$; *** $p < 0.001$; n.s.: not significant.

Supplementary Table 5 – Bridge performance overview, assessed with OPTN: W_1-distance (data from Figure 8B). $p < 0.001$ for each pairwise comparison.

CA3-to-CTX	Disconnected	Bridge-bw5	Bridge-50%	Bridge-100%	Connected
Disconnected		0.1	0.14	0.31	0.52
Bridge-bw5	0.1		0.08	0.21	0.41
Bridge-50%	0.14	0.08		0.17	0.38
Bridge-100%	0.31	0.21	0.17		0.1
Connected	0.52	0.41	0.38	0.1	

CTX-to-CA3	Disconnected	Bridge-bw5	Bridge-50%	Bridge-100%	Connected
Disconnected		0.06.	0.05	0.17	0.12
Bridge-bw5	0.06		0.02	0.12	0.07
Bridge-50%	0.05	0.02		0.12	0.07
Bridge-100%	0.17	0.12	0.12		0.06
Connected	0.12	0.07	0.07	0.06	